ÉCOLE POLYTECHNIQUE PARIS-SACLAY

UNIVERSITAT POLITÈCNICA DE CATALUNYA

Faculty of Engineering

Master of Science in Renewable Energy Science & Technology

Master of Engineering in Energy Engineering

Master Thesis

Impact of TiO$_2$ electron transport layer properties on planar Perovskite solar cells

Alessandro Mercurio

Supervisors:
prof. G. Horowitz
prof. J. P. Gonzalez

Advisor:
Samy Almosni, PhD

September 2017

A mia Madre, per l'affetto donatomi
A mio Padre, cui punto ad assomigliare sempre più

Acknowledgements

Contents

Introduction

During the last century, the energy world consumption have been increasing exponentially due to the development of the societies. Furthermore, the evolution of technologies has gradually unbalanced the equilibrium between the production and the consumption of energy. This led to a tremendous deployment of the natural energy resources such as coal, oil and natural gas, without paying too much attention on possible consequences in terms of environmental effects.

With the first oil shock in 1973, western countries started looking for new kind of energy sources, in order to limit the usage of oil and the dependence on exporter countries. Moreover, in the same period, new ideologies, like environmentalism, started to push up the attention toward a sustainable development. In this historical context, renewable energies seemed to be a good compromise to face these aspects.

Among all the renewable technologies, photovoltaic solar cells are the most promising solution for a low-cost energy production. By the end of 2016 the total installed capacity amounted at least 303 GW corresponding to 1.8% of the global electricity demand. [1]

Solar cells devices can be divided in three main categories: first generation solar cells are mainly based on crystalline silicon wafers (the second most abundant element in the Earth), with performances around 20%. This technology is dominating the market of the solar industry due to the good performances, high stability and strong reduction in cost. Silicon solar cells have a rigid structure that is sometimes considered as a drawback since they can not be used for flexible applications.

The second generation solar cells use the thin-film technology and are mainly based on amorphous silicon, CIGS (copper, indium, gallium, selenium) and CdTe with typical efficiency from 14% up to 22% (CIGS). Important characteristics of these solar cells are the lower material consumption that means a reduction cost of the fabrication process, the lower temperature required during the process, and the possibility (thanks to their thickness) to fabricate them on a flexible substrate. Although the material used is less than in first generation cells, a large amount of energy is still needed during the fabrication process. Additionally, they are mainly based on non-abundant elements (CIGS) and toxic materials (CdTe) that limit their development, especially on the industrial scale.

Third generation solar cells are considered being the most promising technologies for photovoltaic systems. They are developed with the purpose of reducing the cost of energy: for doing this, the objective is to increase the efficiency (multi-junction solar cell) and decrease the costs of material processing (organic solar cells).

This group of technologies includes multi-junction solar cells (employing several layers of

semiconductors in order to absorb the whole solar spectrum and to reduce thermalization) which hold the world record in terms of performances (fig. 1) and a variety of polymers and organic material-based solar cells.

Recently, a new class of thin film solar cells, perovskite solar cells, has attracted the interest of researchers. In only few years since their first application in 2009 with an efficiency of 3%, PSCs showed huge potential, with a record efficiency of 22.1% (not stabilized) achieved in 2016 (fig. 1). [2] This work focuses on the growth of different TiO_2 electron transport material on FTO substrates. The goal is to study the impact of TiO_2 layer properties on the perovskite solar cells with planar structure, in order to respectively reduce the hysteresis and to improve the efficiency.
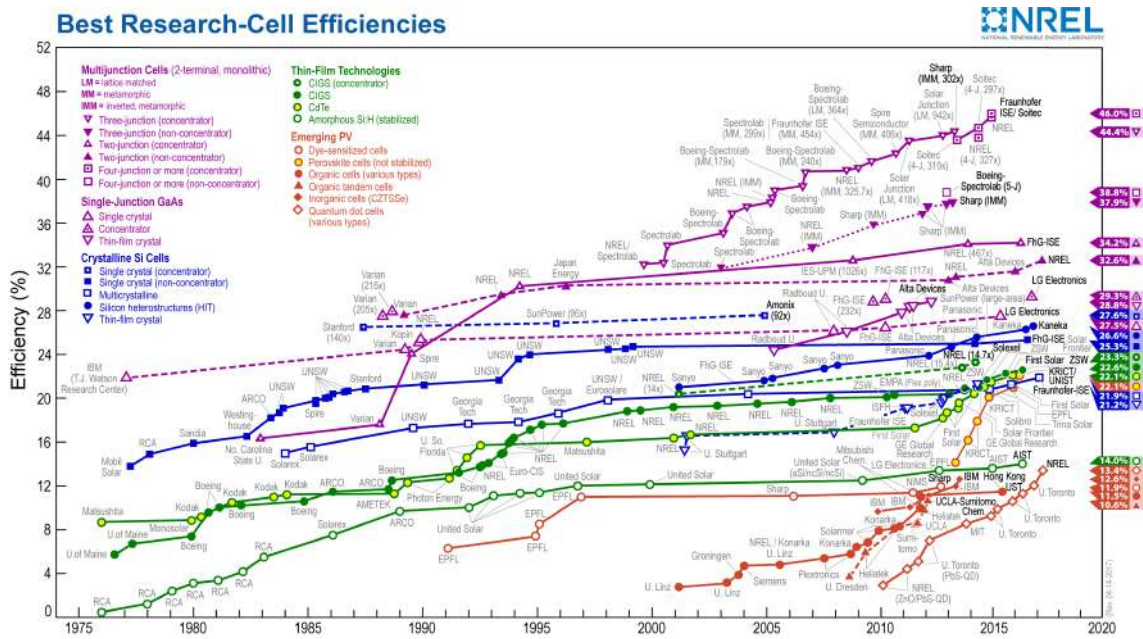

Figure 1: Best research-cell efficiencies chart. This plot is courtesy of the National Renewable Energy Laboratory, Golden, CO.[2]

Chapter 1

Physics of solar cells

1.1 Solar Irradiation

In Physics, a "blackbody" is a body that satisfies three main conditions:

- it is a perfect emitter: for every temperature and wavelength, it emits more radiant energy than other material at the same conditions;

- it is a perfect absorber: it absorbs all energies coming from each direction and at any intensity;

- it is a diffuse emitter: the emitted radiant energy is only function of temperature and wavelength and not on direction.

When a blackbody is in thermal equilibrium (at constant temperature) it emits a certain electromagnetic radiation that is called blackbody radiation. Planck's law, which describes this emitted radiation, states that a blackbody has a spectrum that is univocally determined by temperature [3].
All electromagnetic radiations can be considered as made of particles, known as photon, which carry a specific amount of energy. These particles exhibit also wave properties: in particular, the wavelength is related with the photon energy by

$$E_\lambda = \frac{hc}{\lambda}$$

where h is the Planck constant and c is the speed of light.
The sun, where surface temperatures reach almost 5760 K, emits a radiation that approximates well the one emitted from a blackbody at the same temperature. Although this radiation is almost constant, the amount that reach the Earth's surface is highly reduced because the absorption and scattering in the atmosphere of the planet [3]. The maximum amount of radiation strikes the surface when the sun is overhead (assuming a clear sky) because the optical path length done through the atmosphere by photons is the shortest. This path length can be defined by air mass coefficient:

$$AM = \frac{1}{\cos \varphi}$$

where φ is the angle between the sun and the point directly overhead.

When $\varphi = 0$ the sun is directly overhead. Usually, the international standard for doing a comparison among solar cell performances is the AM1.5 spectrum ($\varphi = 48.2°$), normalized to a total power density of 1 kW/m^2.

Sunlight passing through the Earth's atmosphere is reduced by about 30% before reaching the surface due to effects such as Rayleigh scattering by molecules in the atmosphere (particularly at short wavelengths); scattering by aerosols and dust particles; absorption by atmospheric gases such as oxygen, ozone, water vapor and carbon dioxide (CO_2). Generally, wavelengths below 0.3 μm are strongly absorbed by ozone: depletion of ozone from the atmosphere allows more of this short wavelength light to reach the Earth, with consequent harmful effects on biological systems. Wavelength above 1 μm are absorbed by water vapor and CO_2 [3]. Figure 1.1 shows the spectral power density of the sun: the radiation at the sea level gives an idea on how much the power density of sunlight is reduced by the main atmospheric components.
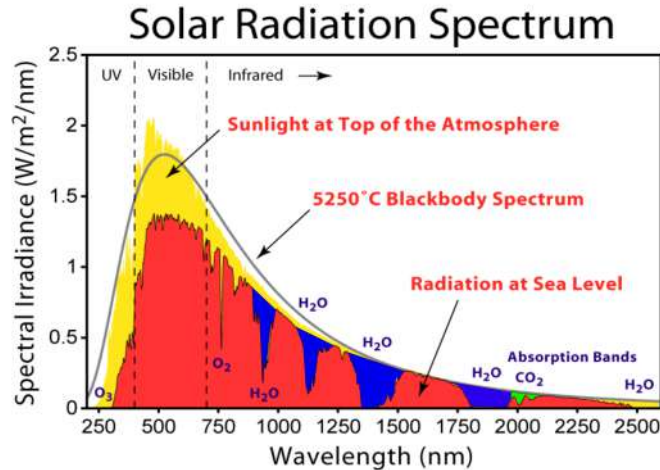
Figure 1.1: Solar irradiation spectrum

1.2   Properties of semiconductors

Solids can be divided into three groups depending on their electrical behavior: conductors, semiconductors and insulators.

The opto-electronic properties of materials depend on the electron configuration that is the distribution of electrons in atomic orbitals. According to the laws of quantum mechanics, the electronic configuration induce band of allowed energy states. Electrons can move from one energy state to the other by the emission or absorption of a quantum of energy, in the form of a photon [6].

Two main states exist: the valence band, when the electron participate in the bonds between atoms, and the conduction band, when the electron is at a high energy level and can be considered free to participate in conduction. The band gap (E_g) is defined as the gap in energy between the bound state and the free state, between the valence band and conduction band [6]. Therefore, the band gap is the minimum change in energy required to excite the electron so that it can participate in conduction.

In conductors, there is no band gap between the valence band and conduction band. The valence band is either not fully occupied with electrons, or the filled valence band overlaps with the empty conduction band. In general, both states occurs at the same time, the electrons can therefore move inside the partially filled valence band or inside the two overlapping bands [4].

In insulators, the valence band is fully occupied with electrons due to the covalent bonds. The electrons can not move because they are strongly bonded between the atoms. Thus, a large energy band gap exist between the valence and the conduction band and only with considerable energy expenditure (if at all possible) the band gap can be overcome; thus leading to a negligible conductivity [4].

In semiconductor the band gap energy is relatively small compared to insulator. Thus, even with a small amount of energy electron can pass from the valence to the conduction band. When an electron gains enough energy to participate in conduction, it leaves behind an empty space in the valence band. This "lack of electron" is called hole, and for convention it assumes the role of positively charged particle that can move through the crystal structure [6]. Also, the energy of the valence and conduction band depend on the electron momentum k. Two main configurations exist either the maximum of E_v and the minimum of E_c happen for the same value of k (direct) or for different value of k (indirect) [6]. Figure 1.2 is a schematic representation of the different band gap in insulator, semiconductors and conductors. Figure 1.3 shows direct and indirect band gap.
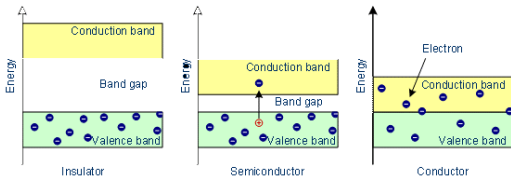
Figure 1.2: Valence and conduction band in insulator, semiconductor and conductor
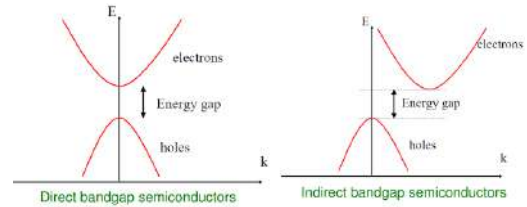
Figure 1.3: Direct and indirect semiconductors band diagram [4]

When light incidents the surface of a semiconductor , photons carrying different amount of energy (depending on the wavelength) interact with the material. Photons with energy (E_{ph}) larger than the band gap (E_g) are absorbed. The amount of their energy equal to Eg is transmitted and it generates electron-hole pairs (carriers). The excess of the carried photon-energy, quantified as the difference between E_{ph} and E_g is lost through thermalization process due to some interaction with a lattice vibration called a phonon [6]. On the contrary, all the photons with lower energy than the bandgap, do not interact

with the semiconductor, passing through it as it was transparent. In direct band gap semiconductors the absorption of photons happens quite easily, because the electron does not need to be given very much momentum. In indirect band gap semiconductors an electron need a significant change in its momentum for a photon of energy E_g to produce an electron-hole pair. This is possible, but it requires such an electron to interact not only with the photon to gain energy, but also with a phonon in order to either gain or lose momentum [5].

The amount of electron-hole pairs per unit volume generated (generation rate) can be estimated by the formula:

$$G = \alpha N_0 e^{-\alpha x}$$

where N_0 is the photon flux (photons per unit area per seconds), x is the distance from the surface of the material and α is the absorption coefficient.

This last is an important parameter that depends not only on the material, but also on the wavelength (inversely proportional) which is being absorbed: it determines how deep a particular wavelength can penetrate into a material before being absorbed. This means that material with a higher α can absorb "quickly" photons. Thus, the absorption depth is equivalent to the inverse of the absorption coefficient and affects in solar cell design, such as the thickness of the semiconductor material. For example: for short wavelengths (such as blue in the visible range), the absorption coefficient α is high and the absorption depth (α^{-1}) is low. This means that blue light is absorbed near the surface of semiconductor while red light is absorbed in the bulk.

Fig. 1.4 shows absorption coefficient for different materials [5].
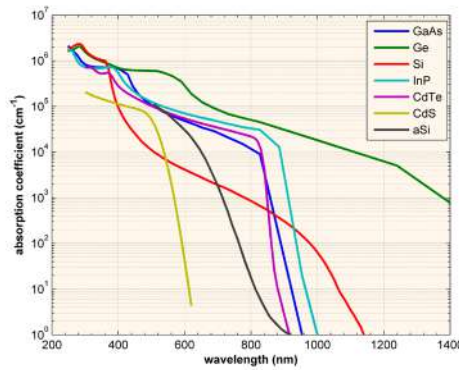
Figure 1.4: The absorption coefficient in different semiconductor materials as a function of the vacuum wavelength of light

When the electrons reach their excitation state in the conduction band, they have the tendency to relax back into the valence band.Such a process is called recombination, since electrons fall from the conduction band to the valence band "recombining" with holes. The three main mechanisms explaining this phenomenon are the radiative (band-to-band)

recombination, the Auger recombination and Shockley-Read-Hall recombination (fig. 1.5) [6]:

- Radiative recombination (band to band) is the inverse of the carrier generation process and it usually dominates in direct bandgap semiconductors. Excited electrons in conduction band while combining with a hole, release their energy as an emitted photon. One of the most explicative example is the light emitting diode (LED). Since during this recombination the photon emitted have an energy near to that of the bandgap, it is possible, with a well-designed direct bandgap solar cell, to reabsorb the same photon before it leaves the semiconductor (photon recycling) [7].

- Auger recombination involves three carriers. When an electron and hole recombine, the energy is given to an other electron in the conduction band. This last carrier then thermalizes releasing its excess of energy as heat [8].

- The Shockley-Read-Hall (SRH) recombination ideally does not occur in pure material without defects. In real devices the concentration and distribution of defects is influenced by the specific growth or processing conditions, impurities, the contact between different interfaces, and so on. These act as a continuum of traps within the forbidden gap: electrons (or holes) can be trapped in these energy state introduced by defects and recombine with the other carrier [9].
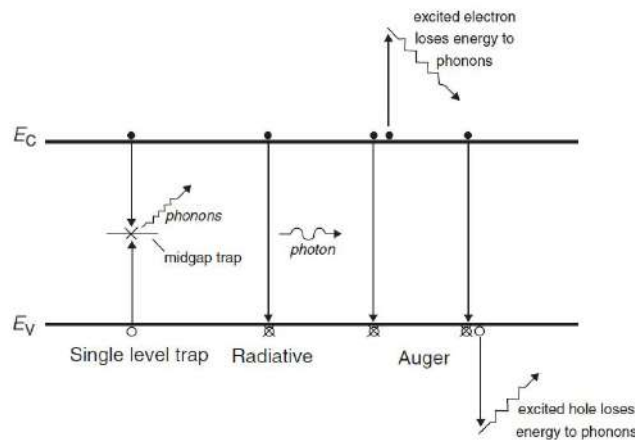

Figure 1.5: Schematic representation of the recombination processes [6]

1.3 PN junction and heterojunction solar cells

In order to design a solar cell some engineering techniques for enhancing the conductivity, the number of carriers, the collection or the transport of the carriers are applied. Among this, the main used, especially for the first generation solar is doping.

Doping is a technique used to vary the number of carriers in semiconductors. In particular, n-type semiconductors are defined as those where the conductivity has been enhanced by increasing the number of available electrons. This is usually done creating intentionally defects or introducing different materials inside the semiconductor: for example, in the case of Silicon, elements from the V elements group of the periodic table, whom atoms have 5 valence electrons are used. These can form covalent bonds with the 4 valence electrons of Silicon atoms. Once the bonds are established, the extra valence electron is free to participate in conduction.

On the opposite, p-type semiconductors are those ones where the number of holes is enhanced.

Considering a doped material, there is always more of one type of carrier (majority carrier) than the other (minority carrier).

When an n-type semiconductor comes into contact with a p-type semiconductor, a pn-junction is formed. Considering that the charge of carriers in the two semiconductors is different, holes diffuse from p-type to n-type and electrons diffuse from n-type to the p-type material depending on the concentration gradients. As the carriers diffuse, they leave behind exposed charges on dopant atom sites, which are fixed in the crystal lattice and are unable to move. On the n-type side, positive ion cores are exposed, while on the p-type side, negative ion cores are exposed. Since this opposite ions are uncovered, an electric field ($\overrightarrow{E_{bi}}$) is produced, which balances the diffusion of the holes and electrons (1.6). The region between the n-type and the p-type semiconductors is known as the space-charge region or depletion region (because it is depleted of free carriers).

As result of the electric field along the space region, a potential difference is established, called built-in potential (V_{bi}).
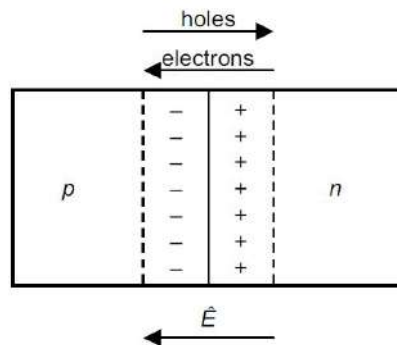

Figure 1.6: When two doped semiconductor form a pn-junction, electric field along the space region is established [6]

The most common semiconductor diode, nowadays, is a PN-junction connected with two terminals: these devices represent the basis not only for solar cells, but also for other kind of systems such as photodiodes, LEDs, lasers.

When the device is at equilibrium, the net current is equal to zero. Indeed, even it might happen that some majority carriers from one side cross the junction due to their high velocity (diffusion current), this is counterbalanced by some minority carriers, on the other side, that reach the edge of the space charge zone and are swept across it by the electric field in the depletion region (drift current).

By applying an external voltage to the device, it is possible to vary the electric field in the junction region. With a forward bias, applying positive voltage to the p-type material and a negative voltage to the n-type material, an electric field is generate in the device, with an opposite direction respect to the one within the depletion region. Thus, the net electric field in the depletion region is the difference between the $\overrightarrow{E_{bi}}$ and the applied field. Considering that in realistic devices the built-in field is always larger than the applied field, a reduction of the net electric field in the depletion region occurs: this disturbs the equilibrium at the junction, decreasing the barrier to the diffusion of the carriers from both sides (fig. 1.7) [10].

While the diffusion current increases, the drift current does not change because it is mainly due to carriers with diffusion length of the depletion region (since the depletion region is slightly reduced, the number of minority carriers swept across the junction do not vary) and this leads to an unbalance between drift and diffusion effects with net current flowing across the junction.

Considering this time a reverse bias (negative voltage to the p-type material and positive voltage to the n-type material) the electric field in the junction region increases with consequential reduction of the probability that carriers can diffuse from one side of the junction to the other (diffusion current decreases).
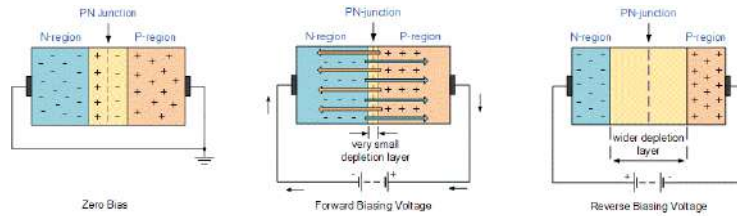
Figure 1.7: The effect of applying a forward or reverse bias in a pn-junction [10]

These phenomena can be described with *the actual diode law*:

$$I = I_0 \left[e^{\left(\frac{qV}{nkT} \right)} - 1 \right]$$

where I is the current, I_0 is the dark saturation current (the diode leakage current density in the absence of light), V is the applied voltage, q is the charge on an electron, k is Boltzmann's constant, T is absolute temperature and n is the ideality factor, a number between 1 and 2 that typically increases as the current decreases.

An evolution of this previous concept is the p-i-n junction, that takes advantage of the fact that in many semiconductor materials, especially direct bandgap semiconductors (with large absorption coefficient), most of the electron–hole pairs are created very near the

surface. Placing an intrinsic (undoped) layer between the n and p regions (usually very thin layers), the depletion region thickness is the most significant fraction of the total solar cell thickness (fig. 1.8) [6]. Carrier collection, in this way, is aided by the electric field in the depletion region
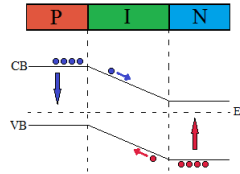
Figure 1.8: Band diagram of a PIN junction [6]

Another kind of design, based on the mismatch in the band diagram, is used in heterjunction solar cells. The purpose od this design is to reduce the recombination losses in the emitter improving though the efficiency of the device. One way is by using a wider bandgap material for the emitter of the solar cell, and highly-doped for an n and p regions. This allows to have a mismatch between the n^+ and p^+ material: the main consequence is that the band structure acts as energy selective contact, preventing the carriers to be collected in the wrong side of the junction and avoiding recombination (fig. 1.9).
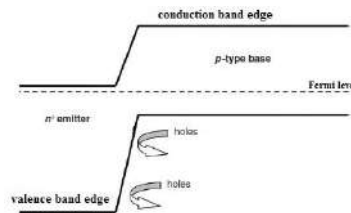
Figure 1.9: Band diagram of a heterojunction junction

1.4 Solar Cell Operation

A solar cell is an electronic device in which a semiconductor materials, can convert directly sunlight into electricity due to the photovoltaic effect.

In this conversion mechanism, as we have seen, two main processes are involved: light absorption, concerning the collection of incident photons and generation of electron-hole pairs, and collection of the carriers due to the electric field in the p-n junction that separate electrons and holes. When a light-generated minority carrier reaches the p-n junction (considering only pn junction for now) it is swept across the junction by $\overrightarrow{E_{bi}}$ and it becomes then a majority carrier in the other side of the junction (drifting current). Connecting the two n and p semiconductor (emitter and base), the carriers flow through the external circuit (fig. 1.10).
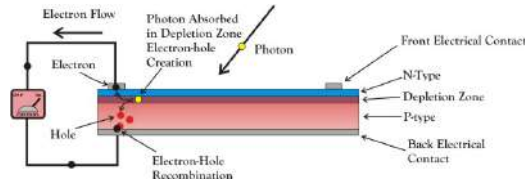
Figure 1.10: Solar cell layout

When the external circuit is open, the light-generated carriers cannot flow through it. As consequence of the collection process, it happens an increase in the number of electrons on the n-type side and an equivalent increase of holes in the p-type material. The accumulation of these charges generate a new electric field that has opposite direction to that one in the junction: as consequence, the net electric field is reduced. The reduction of the electric field increases the diffusion current (as it happens applying an external forward bias).

New equilibrium is achieved because the induced forward bias of the junction increases to a point where the light-generated current (drifting) is exactly balanced by the forward bias diffusion current, and the net current is zero. The voltage required to cause these two currents to balance is called the "open-circuit voltage" [5].

The characteristic curves of a electronic devices are represented by plotting the data in a current-voltage (I-V) graph. In circuit theory the sign of current and voltage through a circuit branch usually follow the passive sign convention: when I and V are both positive (first quadrant), then power is dissipated by the device, as it was a resistive element [6]. When the voltage is positive while the current is negative (fourth quadrant), thus flowing from the cell to the an external load) power is generated by the device. The I-V curves solar cell with and without light incident of the cell surface are shown in fig. 1.11.

Figure 1.11: IV curve

The light has the effect of shifting the I-V curve into the fourth quadrant where power can be extracted from the diode. Considering the light-generated current, the actual diode

law becomes:

$$I = I_0 \left[e^{\left(\frac{qV}{nkT} \right)} - 1 \right] - I_L$$

where I_L is the photocurrent.

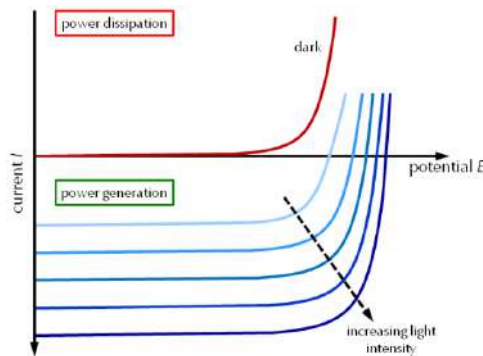The most important parameters for characterizing the I-V curves, thus a solar cell device, are:

- short circuit current I_{sc}: is the maximum current when the voltage is zero. It depends on the generation and collection of the carrier thanks to the light and in ideal device $I_{sc} = I_L$. Even if it strongly proportional to the intensity of light, there are other factors that can affect it, such as the area of the solar cell (indeed is common to consider the current density mA/cm^2), the optical properties of the device (absorption, reflection, transmittance), carrier collection probability, etc.

$$J_{sc} = -q \int_{\lambda_1}^{\lambda_2} EQE(\lambda) \Phi_{ph,\lambda} d\lambda$$

- open circuit voltage V_{oc}: is the maximum voltage when the current is zero. It corresponds to the induced forward bias when light is incident. It increases logarithmically with the intensity of the sunlight. V_{oc} depends also on the saturation current that is correlated with the recombination in the device.

$$V_{oc} = \frac{nkT}{q} \ln \left(\frac{I_L}{I_0} + 1 \right)$$

- fill factor FF: defined as the ratio of the maximum power from the solar cell to the product of I_{sc} and V_{oc}, helps in evaluating the maximum output power of a solar cell.

$$FF = \frac{V_{mp}I_{mp}}{V_{oc}I_{sc}}$$

$$P_{max} = V_{oc}I_{sc}FF$$

Graphically, the FF is a measure of the "squareness" of the solar cell characteristic curve and is also the area of the largest rectangle which will fit in the IV curve.

- conversion efficiency η: defined as the ratio between the maximum output power generated by the solar cell and the incident power coming from the sun.

$$\eta = \frac{P_{max}}{P_{in}}$$

Figure 1.12 shows the electrical scheme of a solar cell diode. The left part of the scheme is the model of the solar cell itself: the diode represents the pn junction, mentioned in the previous chapter, while the current generator represent the photocurrent induced by the light.

R$_s$ and R$_{sh}$ represent the losses of the circuit, defined in terms of series and shunt resistances. The first usually include all those losses due to the contact at the interfaces of different layers on the solar cell, traps and metal contacts. The main impact of series resistance is to reduce the fill factor, and high values may also reduce the short-circuit current.

The shunt resistances are typically due to manufacturing defects such as pinholes. Low shunt resistance causes power losses in solar cells by providing an alternate current path for the light-generated current. In this way, the amount of current flowing through the solar cell junction is reduced, with a decrease also in the output voltage.
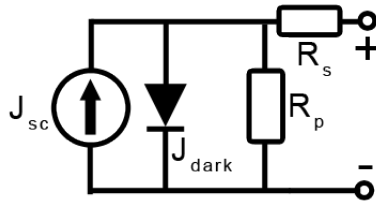
Figure 1.12: IV curve

Chapter 2

Perovskite Solar Cells

Perovskite materials, were studied for the first time in 1839, are described by the stoichiometric formula ABX_3, where X is an anion and A and B are cations of different sizes (A being larger than B) [11].

Perovskite crystals can have many crystallographic structures depending on their composition and temperature. In order to forecast which phase will be the most stable and probably formed, the Goldschmidt tolerance factor t is used. It is defined as the ratio of the distance A-X to the distance B-X in an idealized solid-sphere model ($t = (R_A + R_X)/\sqrt{2(R_A + R_X)}$ where R_A, R_B and R_X are the ionic radii of the corresponding ions) [11]. Generally, around room temperature, if $0.89 < t < 1$ the structure is cubic (fig 2.1), while lower values of t give less symmetric structures (tetragonal or orthorhombic). As said previously temperature also influences transitions between such phases: orthorhombic phase when T < 165 K, tetragonal phase at 165–327 K, and cubic phase with T > 327 K.
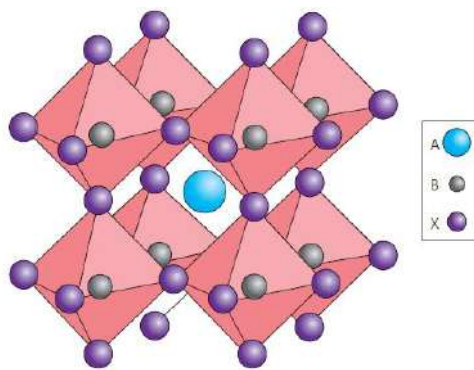
Figure 2.1: Cubic phase of Perovskite [12]

The present study is focusing on organic–inorganic halide perovskites where the larger organic cation A is methylammonium (CH_3NH^{3+} or MA) while the anion X is the halogen Iodine. Br and Cl are commonly used in a mixed halide material (not in the present

work). The cation B is Pb: this has been used by many authors because it is less sensitive than tin-based perovskite ($ASnX_3$) to oxidation [13]. Thus, the compound becomes methylammonium lead triiodide ($CH_3NH_3PbI_3$).

Thanks to the good optoelectronic properties of these materials (absorption, carrier diffusion length and so on), in less than 10 years tremendous improvement has been achieved boosting the conversion efficiency from 3.8% of the first PSC, to 22.1% [2].

Since the first use by the Miyasaka's group [14] of lead halide based perovskite as a light harvester in Dye-Sensitized Solar Cells (DSCs) different approaches have been used to improve their optoelectronic properties and stability. One of the first approach that has led to high efficiency PSCs was to use a solid-type hole transport material (HTM) such as spiro-OMeTAD [15]. Then several optimization steps have been performed, notably introducing an anti-solvent step during the $MAPbI_3$ spin coating leading to smoother perovskite layer having larger grain size [16]. Using this approach efficiency over 18% has been reached. Another strategy was to use mixed halide perovskite introducing Br into $MAPbI_3$ using this approach PCE over 20% has been reach and the device stability has been improved [17]. Recent studies on the $Cs_{0.05}(MA_{0.17}FA_{0.83})_{0.95}PbI_{0.83}Br_{0.17}$ compound have shown the great potential of this alloy by achieving efficiency above 20% with an enhanced device stability and a high process reproducibility [18]. Finally, interesting preliminary results have been recently obtained using perovskite layers having a Ruddlesden Popper structure [19]. Even though the efficiency of these cells is still low (12%) compared to classical architecture, they show promising stability against moisture [19].

This fast increasing of the efficiency, combined with simple processes and fabrication methods, had led to a rapid growth in the number of publication related with this field (fig. 2.2).
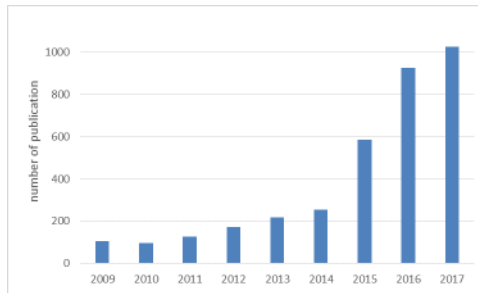

Figure 2.2: Number of publications using the keywords Perovskite Solar Cell on Sciencedirect.com

2.1 Properties of PSC

The comprehension of the optoelectronic properties of halide perovskite is important to develop more efficient photovoltaic devices. Even if many efforts have been done in order to explain the mechanisms that regulate the carriers generation under illumination of this

kind of material, the functioning of PSCs is still debated [11].

It has been determined that MAPbI$_3$ is a direct bandgap material (1.6 eV). Absorption coefficients of MAPbI$_3$ and MAPbI$_3$:Cl were evaluated by several groups: with its band edge at 780 nm, a thin film of perovskite, with a thickness around 400 nm, is able to absorb all of the visible spectrum [20]. This strong optical absorption is one of the key-points that attracts interest on this material. It means that it is possible to reduce the amount of material used maintaining a high efficiency. (fig. 2.3) [11].
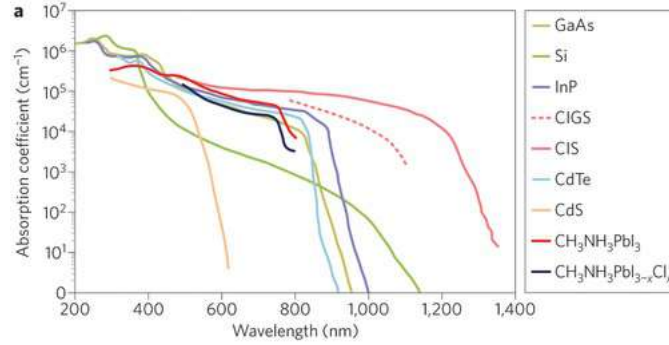
Figure 2.3: Comparison between absorption coefficient of the perovskite of other materials

Another interesting property strongly related with the optoelectronic device performances is the long carrier diffusion length [11]. Furthermore, perovskite is also less sensitive to impurities than other expensive crystalline semiconductors such as gallium arsenide [11]. Concerning solar cell devices, many different architectures have been realized [11]. The two main structures, presented in figure 2.4, are:

- the mesoporous structure: a transparent electrode (one of the most common is Fluorinated-Tin Oxide, FTO) is covered by a thin layer of TiO$_2$ (usually 30 nm). A mesoporous scaffold is deposited on top. Perovskite solution is then deposited: during the thermal treatment, the amount of solution that fills the pores, forms small crystals with a constrained growth [21]. On top, the remaining amount of solution forms a layer of big crystals called the "capping layer". Finally, the hole extraction layer is deposited (generally spiro-OMeTAD). This structure, FTO/c-TiO$_2$/ mp-TiO$_2$/Perovskite/spiro-OMeTAD, allows to have an important reduction in term of hysteresis, as it will be explained in next section. Although this, the fabrication process remains long and more complex.

- the planar structure: there is no mesoporous scaffold and the layers are stacked one over the other simplifying the fabrication process. Generally an high hysteresis is observed. This group of planar cells is divided in two sub categories: standard or inverted structure (the definition is a convention based on the direction of the photocurrent).
The first one is similar to the mesoporous structure, but without the scaffold (FTO/TiO$_2$/ Perovskite/HTL). Usually, high performances are achieved with this configuration [11]. The inverted configuration, that shows less hysteresis, uses different interlayers: the hole

transport layer is PEDOT:PSS and is deposited on top of the transparent conductive electrode (ITO). The electron extraction layer is a film of PCBM deposited on top of the perovskite. Due to the high reactivity of PCBM anions, layers of metal oxides nanoparticles like Zinc Oxide (ZnO) or TiO_2 are often used to protect the layer from degrading agents [22].

During the development of this thesis project, we focused mainly on planar standard configuration that has the following structure FTO/c-TiO_2/Perovskite/spiro-OMeTAD.
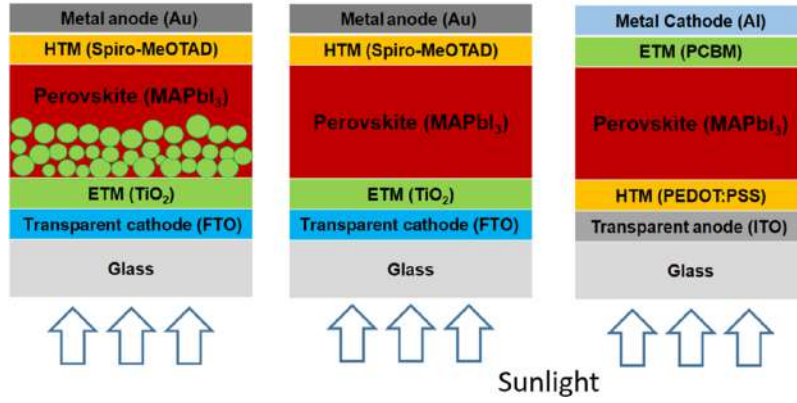
Figure 2.4: From left to right: mesoporous structure, standard planar structure, inverted structure.

2.2 Stability of Perovskite solar cells

Although the good properties mentioned before, the stability of PSCs is still a big issue. Indeed, it is fundamental that the performances remain quite stable for more than 20 years to be attractive from an industrial point of view.

Many studies reported moisture as the most dangerous agent for perovskite materials since it leads to an irreversible degradation of the active layer. The simplified chemical decomposition can be summarized as:

$$CH_3NH_3PBI_3 \rightleftharpoons CH_3NH_3I(aq) + PbI_2(s)$$

$$CH_3NH_3I(aq) \rightleftharpoons CH_3NH_2(aq) + HI(aq)$$

$$4HI(aq) + O_2 \rightleftharpoons 2I_2(s) + 2H_2O$$

$$2HI(aq) + h\nu \rightleftharpoons H_2 + I_2(s)$$
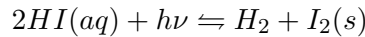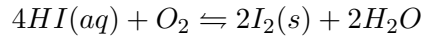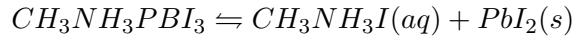
where it is indicated that HI and MA are soluble in water.

An unsafe consequence of this degradation is due to one of the products that come out

from the reactions: PbI_2 being soluble in water, could contaminate the environment, polluting the field and causing eco-toxicological disasters. Oxygen can also cause degradation of the device. Murphy's group compared different samples stored in dry air and under nitrogen atmospheres. They pointed out that the diffusion of molecules activated by UV illumination promote the formation of peroxide or superoxide compounds which degrade the active layers [23].

UV light can also affect the TiO_2 compact layer of the device during long-term operation. Indeed, it was shown that UV might create deep traps in TiO_2 [11].

One last stability issue, is the thermal stability. Crystallographic structure is sensitive to temperature, and degradation of the active layer can happen after exposing the device at elevated temperatures for medium-long time [11]. MCGee's group showing that their cell are stable at 80 °C for more than 1000 hours.

2.3 Hysteresis

Another major problem is the hysteresic behaviour observed in current and voltage curves [24].

This phenomenon is a notable mismatch between the measured forward (from negative to positive voltage) and backward J-V scan (from positive to negative voltage). The main consequence is the difficulty to determine the device efficiency. One example of this problem is shown in figure 2.5, considering real data of a solar cell fabricated for this thesis project. In this device, the backward efficiency is 16.67% and the forward 9.65%
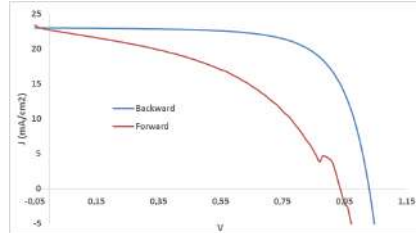
Figure 2.5: Standard planar MAPbI3 J-V curves

Hysteresis in J-V curves has been observed in other kind of devices using fast scan rate, such as dye sensitive solar cells, organic thin film solar cells or Si solar cells. In this case, the phenomenon is due to the effect of capacitive charges (space charges and trapped charges). Since the scan rate is faster than the release-rate of traps, or faster than the space charge relaxation time, hysteresis behavior is seen [24].

In case of PSCs, hysteresis is much more complex and still needs to be understood. Indeed, it is affected by many factors such as conductivity of perovskite or the architecture of the device [24].

Park et al., and many other groups reported that devices with the same perovskite composition but with different architectures (different ETL and HTL) show various levels of hysteresis. Standard planar heterojunction architecture, for example, often show large

hysteresis while inverted architecture with PCBM as the electron collecting layer exhibits very low hysteresis (depending on the thickness of PCBM) [25].

Moreover, other groups obtained TiO_2 meso-structure devices having less hysteresis (depending on the thickness of the scaffold) than the planar heterojunction cells [25].

Since perovskite solar cells are very sensitive to the processing conditions, even devices with the same architecture but fabricated by different person or in different laboratories can show different results. Any small change in the device structure, or of the environment (humidity, temperature, and so on) during the fabrication process, can alter the carrier collection at the electrodes and consequently bring changes in the J-V hysteresis.

Although many efforts have been done to understand the origin of this phenomenon during recent years, at the present there is still not a universal accepted mechanism that explains it.

Some of the most recent studies, still under big debate, are attributing the origin of the hysteresis to:

- perovskite ferroelectric property: Stoumpos et al. [26] found that organo-trihalides of Pb (for example $CH_3NH_3PbI_3$) exhibit hysteretic polarization-electric field due to polarization of domains under external bias potential.
  They observed that doing poling of the PCS (polarization by prebiasing in dark), hysteresis of J-V curves is enhanced. This is attribute to polarization of the ferroelectric domains that leads to modification of band structure at the interfaces. Although, these authors tried to evidence the effect that ferroelectric property has on the phenomenon, other authors still contradict this thesis that assumes ferroelectric polarization is the main cause of hysteresis.

- ions migration: PbI_2 ionic crystals (and also compound derived from PbI_2 such as perovskite) have high-density of mobile halide ions, which can diffuse freely in crystals through existing vacancies either due to the influence of light or to an applied bias.
  Furthermore, it was noticed that in perovskite not only lead has a mobility but even the organic group cations: in particular, the halide anions (which are smaller than Pb^{2+}) can diffuse faster.
  The general idea behind the theory of ions migration is that by biasing the solar cell, anions and cations are accumulated at the ETL and HTL interfaces (near the respective electrodes). This polarizes $MAPbI_3$ enhancing photocurrent generation. Nevertheless, at the present the ions migration process is still not clearly understood and there are no studies directly correlating hysteresis with ions migration. Furthermore, some contradictions with this theory were found. Indeed using the same $MAPbI_3$ perovskite crystal (expecting to exhibit the same ions migration and thus hysteresis) but with different ETL and HTL, PSCs showing different hysteresis have been obtained [24].

- interfacial carrier dynamics: Jena et al. reported hysteresis behavior in a cell fabricated with non-ferric PbI_2 [27]. This obviously implicates that ferroelectric property cannot be the only cause originating hysteresis. Moreover, they analyzed the I-V curve in simplified structures (such as $FTO/TiO_2/Spiro-OMeTAD/Au$ and FTO/TiO_2) evidencing that the interface between FTO and TiO_2 can be one of the contributors to hysteresis [27].

It is known that almost any modification at the interface between perovskite and ETL affects the hysteresis: for example, the incorporation of C60, Zr or Au nanoparticles on TiO_2 [28] can reduce the hysteresis.

Another mechanism probably at the origin of the hysteresis is the unbalanced carrier extraction rate between HTL and ETL. The main evidence of this was found in inverted architecture using PCBM as electron collector. This last is much more conductive (0.16 mS/cm) than TiO_2 (6×10^{-6} mS/cm) and it has a more balanced carrier extraction (hole extraction rate $\approx$ electron extraction rate). Using this architecture, PSCs showed a strong reduction of hysteresis [29].

An unbalanced carrier extraction rate can also be a consequence of accumulation of the carriers at the layers interfaces due to structural defects or the presence of energetic barrier between the materials.

- trap states: another possibility regarding the origin of the hysteresis is related with the presence of traps at the interfaces of the layer or at grain boundaries of perovskite. Almosni et al. [30] proposed a model, valid for both planar and porous structures, explaining that the hysteresis is due to the tunneling assisted trapping of carriers at the interface between TiO_2 and $MAPbI_3$. The intensity of hysteresis in case of porous and planar cells, depends on the concentration of deep traps in the device.

Chapter 3

Characterization and fabrication process

In this chapter, characterization techniques and fabrication processes used for the experiments of this thesis will be described. Since PSCs are sensitive to pre-condition and to the environment, all the characterizations were mainly done right after the end of the fabrication process. All the samples were stored in a dry-room (25 °C and 30% relative humidity).

Firstly, the different characterization techniques (electrical, structural and optical) will be introduced. Then fabrication process used as baseline for the comparison will be described.

3.1 Electrical characterization

The electrical characterization of solar cells is a fundamental tool that easily gives information about device performances. All the parameters such as J-V curves, efficiency, short circuit current, open circuit voltage, fill factor, quantum efficiency and so on, can be determined. In order to simulate the sunlight spectra, different sources can be used, according to their relative cost, illumination area, spatial uniformity, temporal stability, and spectral irradiance [31].

The current-voltage characteristics of the perovskite solar cells fabricated for this work were evaluated with an AM 1.5 solar simulator (CEP-25TF, Bunkoukeiki Co., Ltd, fig. 3.1). The irradiation source was Xe + Halogen lamp for monochromatic light was used for the EQE measurements, while a simple Xe lamp with white light bias for the J-V measurements. The measurements were done at room temperature, using a scan rate of 0.2 V/s and an active area of the solar cells of 0.0314 cm^2.

The light intensity was calibrated by a standard silicon cell (BS-520 S/N 235, Bunkoukeiki Co., Ltd). Data were collected by source meter (Keithley 2400).

Figure 3.1: Solar simulator CEP-25TF, Bunkoukeiki Co., Ltd

3.2 SEM

Scanning electron microscope (SEM) is a type of electron microscope that produces images of a sample by scanning the surface with a focused beam of electrons. It is useful in order to observe the film morphology directly, having information about grain structure, grain size, uniformity of the layers coverage [32]. In the most common SEM, a beam of electrons is produced at the top of the microscope by an electron gun. The beam is sent to the sample following a vertical path, passing through magnetic lenses. When the beam interact with the sample, this latter emits electrons and X-rays. Different detectors collect those signals coming from the sample and convert them in a high-resolution image [32]. Figure 3.2a shows a scheme of standard SEM [33].

Different types of signal are produced and detected such as secondary electrons (the most common), reflected or back-scattered electrons (BSE), X-rays and light cathodoluminescence (CL), absorbed current (specimen current) and transmitted electrons [32].

Since SEM needs vacuum condition and uses electrons to form an image, special preparations of the samples are required. All non-metals need to be made conductive by covering the sample with a thin layer of conductive material. All metals are conductive and require no preparation before being used [33].

In the present work a Hitachi SU-8000 scanning electron microscope, fig. 3.2b, in the Segawa Laboratory (University of Tokyo) was used. Before starting the analysis, the samples were covered with a thin layer of Platinum/Palladium to minimize the charging effect.

Figure 3.2: A - scheme of a standard SEM; B - Hitachi SU-8000 scanning electron microscope

3.3   XRD

X-ray diffraction (XRD) is a rapid and non-destructive technique to determine the atomic structure of crystalline materials. Among the X-ray crystallography methods, XRD is the oldest and the most precise one when used for single crystal analysis [34]. X-ray production generally involves bombarding a metal target in an x-ray tube with high speed electrons, accelerated by tens to hundreds of kilovolts of potential. The bombarding electrons can eject electrons from the inner shells of the atoms of the metal target. Those vacancies will be quickly filled by electrons dropping down from higher levels, emitting x-rays with sharply defined frequencies associated with the difference between the atomic energy levels of the target atoms [35].

XRD measurement is based on the principle that crystal lattice of non-amorphous material are, generally, regular arrays of atoms. When an incident X-ray beam encounters the crystal lattice, scattering occurs and spherically spreading waves are formed. Although most scattering interferes with itself and is eliminated (destructive interference), diffraction occurs when scattering in a certain direction is in phase with scattered rays from other atomic planes [34]. Under this condition, the reflections combine to form new enhanced wave fronts that mutually reinforce each other (constructive interference). The relation by which diffraction occurs following the Bragg law:.

$$n\lambda = 2d\sin(\theta)$$

where n is the order of the interference, λ is the wavelength of X-rays, d is the lattice spacing and θ is the angle of incidence (as schematize in figure 3.3a) .
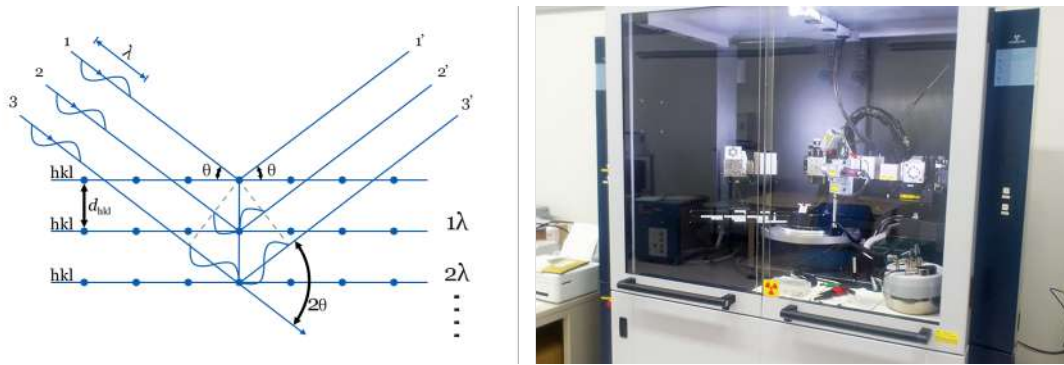
Figure 3.3: A - scheme of Braggs law; B - Solar simulator CEP-25TF, Bunkoukeiki Co., Ltd

Since each crystalline material has a characteristic atomic structure, it will diffract X-rays in a unique characteristic pattern. A detector collects the X-rays reflected. The signal is electronically processed and converted into a count rate. Changing the angle between the X-ray source, the sample, and the detector at a controlled rate an X-ray scan, or diffractogram, is elaborated.

The XRD diffractometer are calibrated in terms of 2θ which is the angle between the diffracted beam and the non-deflected beam [34]. In this study, the diffraction pattern of MAPbI$_3$ solar cell and of different TiO$_2$ films were detected with a Bruker D8 Discover, figure 3.3b, at the Segawa Laboratory (University of Tokyo), using Grazing Incident XRD and $\theta/2\theta$ XRD. Figure 3.4 shows different XRD diffractograms for bare FTO, TiO$_2$ on top of FTO and a complete solar cell.
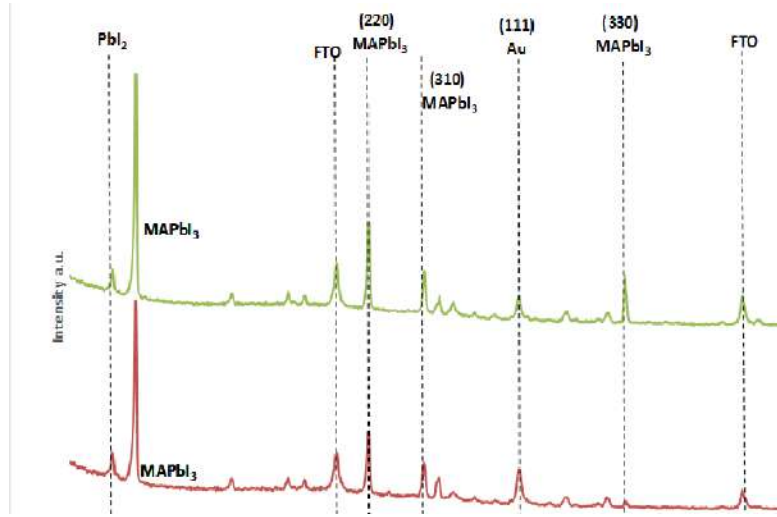
Figure 3.4: XRD diffractograms of bare FTO, TiO$_2$ coated on top of FTO, Perovskite

3.4 Photoluminescence

Photoluminescence (PL) is one of the most used non-destructive technique for optical characterization of solar cells. PL can be used to study the band gap, thermalization and recombination processes of a material.
When a sample is irradiated with high energy light source, photons are absorbed, and electrons and holes are formed in the conduction and valence bands, respectively. The excited carriers firstly relax back toward the band gap minimum, then can recombine emitting photons. As seen in previous sections, recombination mechanisms vary with the material properties. In the case of direct band gap material, like perovskite, the recombination energy of the excited electron-hole pair will be converted into non-radiative or radiative emission which is equal to the band gap energy [36]. Since the generated photon is consequence of a recombination process, it can be related to defect sites or traps.
In our work, we used the PL characterization (Nd:YAG laser Continum's Minilite, with laser light at 532 nm, or higher harmonics at 355) to study the optical properties and defect of different TiO$_2$ compact layers grown on bare glass substrates. Figure 3.5a shows a scheme of PL setup.
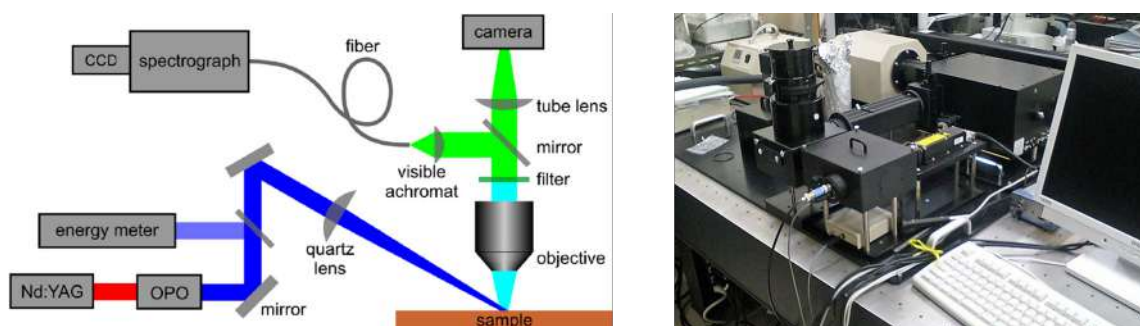
Figure 3.5: A - photoluminescence setup; B - YAG laser Continum's Minilite

3.5 Ultraviolet-visible spectroscopy

Ultraviolet–visible spectroscopy (UV-Vis) is a method used in photovoltaic industry to evaluate optical properties (such as reflectance, index of refraction, extinction coefficient) of a device through the measured spectral range. The instrument used for these evaluation is called spectrophotometer.

A first beam of light from a visible-UV source such as tungsten filament (300-2500 nm), deuterium arc lamp (190-400 nm), Xenon arc lamp (160-2,000 nm) is split by a prism or diffraction grating [37]. One beam pass through the sample while the other beam is used as reference. The intensities of these light beams are then measured by electronic detectors and compared (as schematized in fig. 3.6a). The intensity of the reference beam, is defined as I0. The intensity of the sample beam is defined as I. The ratio between these two values $T = I/I_0$ is called transmittance, while the absorbance is defined as $A = \log I_0/I$. In this thesis, the UV-vis measurements were done to do a qualitative analysis of different TiO_2 compact layer grown on bare glass. The tool used was Shimadzu's new UV-3600 Plus UV-VIS-NIR spectrophotometer (fig. 3.6b).
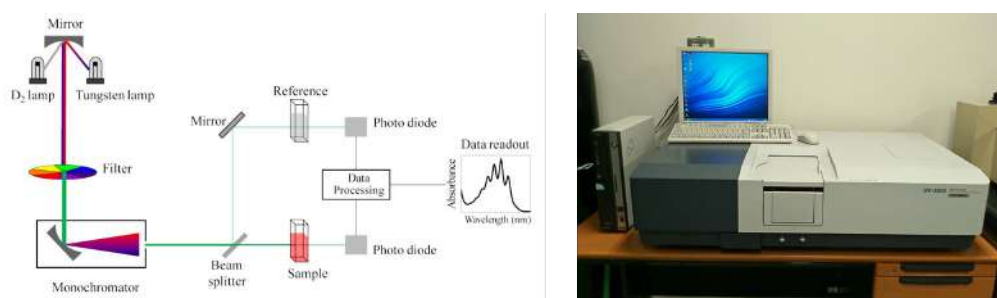
Figure 3.6: A - ultraviolet-visible spettroscopy setup; B - UV-3600 Plus UV-VIS-NIR spectrophotometer

3.6 ALD

Atomic layer deposition (ALD) is a deposition technique used during the fabrication process that allows to grow a variety of thin film materials from the gas phase. The majority of ALD reactions use two chemicals reactants, called precursors [38]. This deposition method is considered to be very promising due to the potential for producing very thin film with a desired thickness and composition. There results can be achieved thanks to the cyclic, self-saturating nature of ALD processes [38].

During a typical ALD process, the substrate is exposed to two precursors A and B in a sequential, non-overlapping way. Each reactant reacts with the surface in a self-limited way: the reactant molecules can react only with a finite number of reactive sites on the surface. When all the reactive sites have been consumed, the growth interrupts. The remaining amount of reactant is pumped away. Then the system allows the reactant B to get into the reactor [38]. The time between the flow-in and the flow-out of one reactant is defined cycle. Figure 3.7 shows the scheme of growth phases during one cycle.

The growth of a layer can be described with the formula: $R_{ads} = SF$, where R_{ads} is the rate of adsorption of the precursor on top the substrate, S is the sticking probability, and F is the incident molar flux [39].

In the present work, a GEMStar XT™ Benchtop Thermal ALD System in the Segawa Laboratory (the University of Tokyo) was used to deposit different thickness of Al_2O_3 using trimethylaluminum (TMA) and H_2O as precursors.
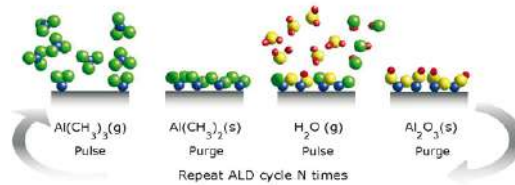
Figure 3.7: Sequential cycles during ALD deposition

3.7 Solar cell fabrication

The process starts with the preparation of the Fluorine doped Transparent Oxide substrates, which are etched with a laser beam to obtain the required electrode pattern. After that, the FTOs are cleaned with distilled water, ethanol and acetone (ten minutes for each step) using an ultrasonic bath cleaner for removing all the organic and inorganic contaminants.

On top of the cleaned substrates the TiO_2 compact layer, 250 mM titanium diisopropoxidebis(acetylacetonate) solution (Aldrich), diluted in high grade anhydrous ethanol, is deposited by spray pyrolysis at 500 °C. Then the TiO_2 precursors anneal on a hot plate at 500 °C for 20 min. After the cooling down, UV Ozone treatment is applied.

After that, the perovskite film is deposited. The perovskite solution is prepared dissolving

CH$_3$NH$_3$I (MAI) powder and PbI$_2$ powder (1:1 molar ratio) in a mixture of DMSO and DMF (1:3 v/v) and then stirred for 10 min. The resulting solution is coated onto the c-TiO$_2$/FTO substrate by a two consecutive step process at 1000 and 6000 rpm for 10 and 25 s respectively. During the second coating step (at 6000 rpm), each substrate is treated with 1 mL of toluene drop-casting. The films then anneal at 100 °C for 1 h in air.
The hole transport material, spiro-OMeTAD (Solarpur), dissolved in chlorobenzene (53 mM), is spin coated at 4000 rpm for 30 sec. Before thermal depositing the gold electrodes using a joule evaporator (in vacuum at 4x10^{-4}), the substrates are let in the dark overnight at room temperature and 30% relative humidity to allow the oxidation of Spiro.
Figure 3.8 shows the final planar architecture of the device.
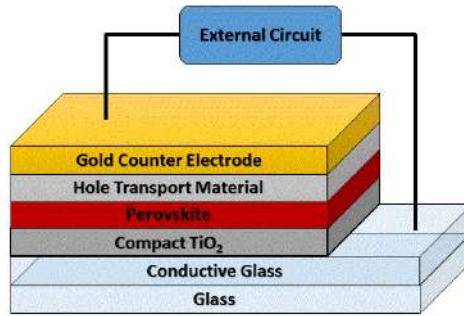
Figure 3.8: Planar standard architecture of MAPbI$_3$ solar cell

Chapter 4

Experimental results and discussion

In this chapter the experiments performed will be presented and discussed.

4.1 Baseline solar cells

The fabrication process for the baseline solar cells was introduced in the previous section. The main issue was to obtain a good reproducibility of the results. Figure 4.1 shows the average JV curve for baseline solar cells. It is clearly visible that they suffer of a large hysteretic behaviour. Furthermore, series resistances affect negatively the right part of the curve, decreasing the FF and consequently the efficiency.

	backward	forward
Jsc [mA/cm2]	21,17	19,86
Voc [V]	0,88	0,84
PMax [mW/cm2]	9,77	3,62
Vmpp [V]	0,61	0,38
Impp [mA/cm2]	16,01	9,53
Fill Factor	0,53	0,22
Efficiency [%]	9,77	3,62
Hysteresis Factor	0,63	-
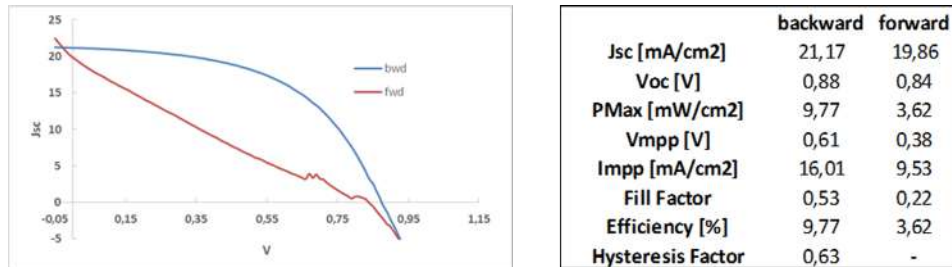
Figure 4.1: J-V curves of PSCs fabricated with spray pyrolysis deposition

The lack of reproducibility was related with the TiO_2 deposition by spray pyrolysis. Since this process was not automatized, it was sensitive to operator-related factors such as the distance between the spraygun noozle and the samples, spraying time/regularity.
We performed structural characterization of the samples. As shown by the SEM in figure 4.2a, the HTL and Perovskite layer are around 90 and 200 nm respectively. In this case, the resolution of the tool does not allow to estimate the TiO_2 compact layer thickness. Such a thin ETL layer could not be sufficient to have a proper carrier extraction rate.

This last assumption was confirmed by the time-resolved photoluminescence characterization. In figure 4.2b we studied the PL decay of a baseline solar cell and a simple $MAPbI_3$ layer coated onto a bare FTO. As the time resolve photoluminescence (tr-PL) shows, the decay time of the two samples is comparable. Thus, this can be interpreted as the TiO_2 layer is not acting as ETL efficiently because of the thickness.
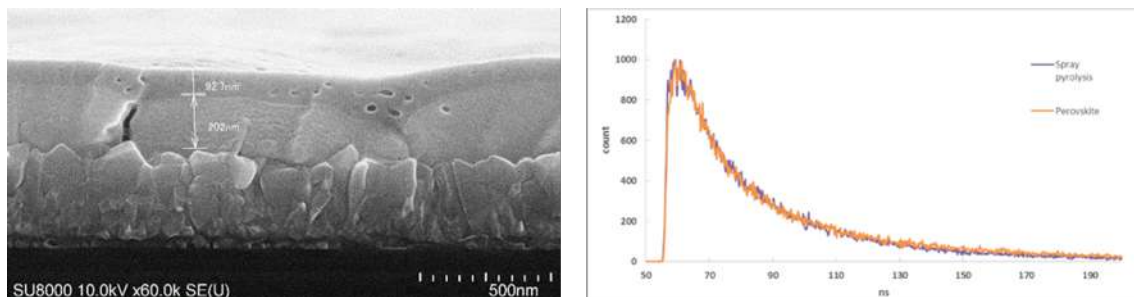
Figure 4.2: A - Sem showing different layers. The cp-TiO_2 is not clearly visible. B - Time resolved photoluminescence

4.2 TiCl$_4$ surface treatment

To obtain a more reproducible and homogeneous ETL layer the spin coating deposition method of the TiO_2 was tested. The same solution of the regular recipe is now spin coated on top of the FTO substrates at 3000 rpm for 30 seconds. The TiO_2 precursors are dried at 120 °C for 10 minutes in air and then rapidly cooled at room temperature. After the same process is repeated a second time, the samples are heated at 500 °C for 1 hour into a furnace.

The final homogeneous thickness of the TiO_2 compact layer is about 50 nm.

For further enhancing device performance, and reducing the hysteresis a $TiCl_4$ treatment, before the deposition of the perovskite layer, is done. This kind of treatment has been mostly applied in DSCC [40] and and in PSC [41].

After the cooling down of the furnace, the TiO_2/FTO substrates are immersed in an aqueous $TiCl_4$ solution (90 mM $TiCl_4$ diluted in distilled water) at 70 °C for 60 min, and then rinsed with methanol. After this, the calcination step is done at 500 °C for 1 h in furnace: such high temperature allows to remove organic components.

Then, the perovskite film, HTL and gold electrode are deposited as in the previous process. Figure 4.3 shows the progress in reproducibility and the improvement of the devices performances due to the $TiCl_4$ treatment.

Considering the average values, the photocurrent remained almost unchanged (or slightly decreases) while an important improvement can be seen in V_{oc} and in Fill Factor, with a consequently improvement of the backward efficiency. It has been already demonstrated that $TiCl_4$ treatment at low temperature of the TiO_2 layer can increase the conductivity, and lower overall series resistance (decreasing of charge recombination kinetics) [42].

29

	without TiCl4	with TiCl4	Δ
Jsc [mA/cm2]	22,12	21,47	-3%
Voc [V]	0,80	0,90	12%
P Max [mW/cm2]	7,94	12,09	52%
Vmpp [V]	0,48	0,69	43%
Impp [mA/cm2]	16,36	17,62	8%
Fill Factor	0,44	0,62	41%
$\eta_{backward}$ [%]	7,94	12,09	52%
$\eta_{forward}$ [%]	2,66	8,33	-
Hysteresis factor	0,67	0,31	-53%
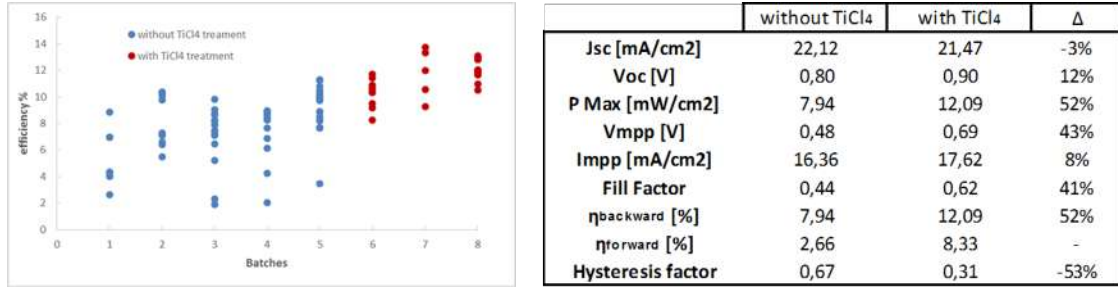
Figure 4.3: Performances of MAPbI$_3$ solar cells with and without the TiCl$_4$

The SEM of the solar cell is shown in figure 4.4. The TiO$_2$ compact layer is clearly visible and seems to cover well the FTO surface with a homogeneous thickness of approximately 40 nm.
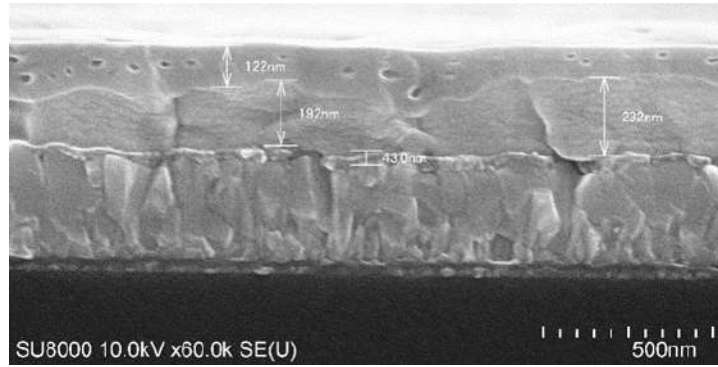
Figure 4.4: SEM shows cp-TiO$_2$ covering well the FTO

In conventional planar PSCs it was shown that the surface treatment of the compact TiO$_2$ layer with TiCl$_4$ is related to a better interfacial adhesion between compact TiO$_2$ and perovskite layer [41]. This highlights the crucial role of the properties of the at layers interface.

A notable reduction in term of hysteresis was observed. To evaluate it, a hysteresis factor $0 < HF < 1$ was introduced, defined as:

$$HF = \frac{\eta_{\text{(backward)}} - \eta_{\text{(forward)}}}{\eta_{\text{(backward)}}}$$

When the values of HF is close to 0, it means that the backward and forward I-V curves are almost the same and the hysteresis is low. On the contrary, when the value is close to 1 the hysteresis is larger.

In order to investigate the light soaking (L.S.) effect, that is typically affecting planar

30

perovskite solar cells, the performance of the devices was tested also under continuous illumination.

Indeed, just before measurement, the devices were stored in the dark without applying any external bias. We defined the condition under which the devices are measured immediately after exposure to the solar simulator as 'without light soaking' and the condition under which the device is measured after reaching saturation with exposure to light (usually between 60 to 120 seconds of continuous illumination) as 'with light soaking'.

Figure 4.5 shows the J-V curve and the relative data for one perovskite solar cell treated with $TiCl_4$ with and without light soaking.

Without Light Soaking			With Light Soaking		
	backward	forward		backward	forward
Jsc [mA/cm2]	21,69	21,49	Jsc [mA/cm2]	21,57	21,41
Voc [V]	0,913	0,917	Voc [V]	1,03	0,95
PMax [mW/cm2]	12,87	9,3	PMax [mW/cm2]	16,09	10,42
Vmpp [V]	0,7	0,6	Vmpp [V]	0,84	0,67
Impp [mA/cm2]	18,39	15,51	Impp [mA/cm2]	19,15	15,55
Fill Factor	0,65	0,47	Fill Factor	0,72	0,51
Efficiency [%]	12,71	9,3	Efficiency [%]	16,09	10,42
Hysteresis Factor	0,27		Hysteresis Factor	0,35	

Figure 4.5: Backward and forward voltage scan with and without L.S.

When the device reached the saturation under continuous irradiation, the performance was enhanced. The most affected parameter was the V_{oc} with an increment of the 13% with respect to the same device but measured without light soaking. Both the Fill Factor and efficiency increased. The mechanism regulating the light soaking effect is still not completely clear and under debate.

Stranks et al. [43] attributed this effect to traps in the perovskite absorber layer after they performed some photoluminescence studies, while Heo et al. [44] attributed it to the surface trap in TiO_2 ETL.

Shao el al. [45] investigate on their planar perovskite solar cells using the impedance spectroscopy. From the Nyquist plot they assumed the presence of chemical capacitance (due to accumulated electrons), probably associated with the occupancy of the trap states at the Perovskite/ETL interface. This chemical capacitance was significantly reduced after the devices reached the saturation due to light soaking, indicating a lower number

of available carrier traps at the Perovskite/ETL interface.

Figure number 4.6 shows the grazing incidence xrd diffractogram. The peaks related to FTO (especially the one in 2-theta=34°) are reduced in $TiCl_4$ treated cells. This is probably related to thicker and more homogeneous $cp\text{-}TiO_2$ in treated samples (the homogeneity depends also on the roughness of the FTO substrate). The Full Width at Half Maximum (FWHM) of the peaks give an estimation about the gains size. Since in this case the FWHM values are comparable, it means that crystallinity is not affecting the device's performance. Figure 4.7 shows the steady-state PL and tr-Pl spectra: $TiCl_4$ treatment decreases the emission spectra of PSCs. This can be a consequence of two main factors: a better carrier extraction due to the treatment, shown in the PL spectra and a higher non-radiative recombination that reduces the carrier lifetime of no-treated samples, as shown in tr-PL.
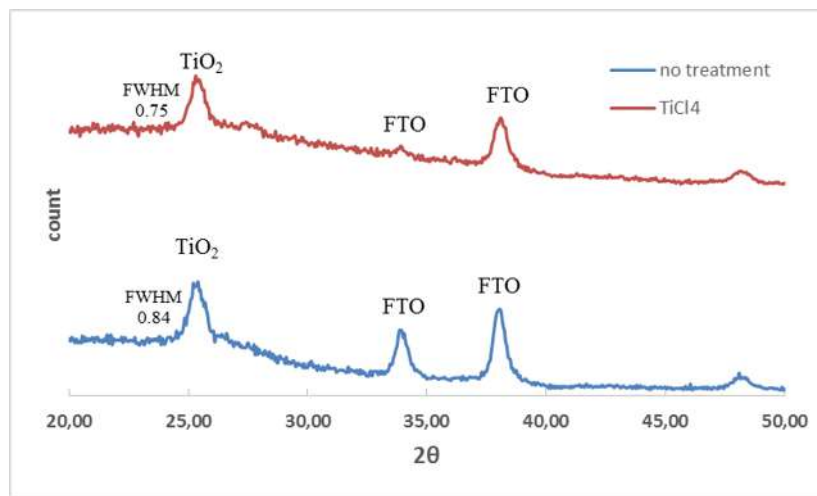

Figure 4.6: Grazing Incidence XRD comparing treated and untreated PSCs
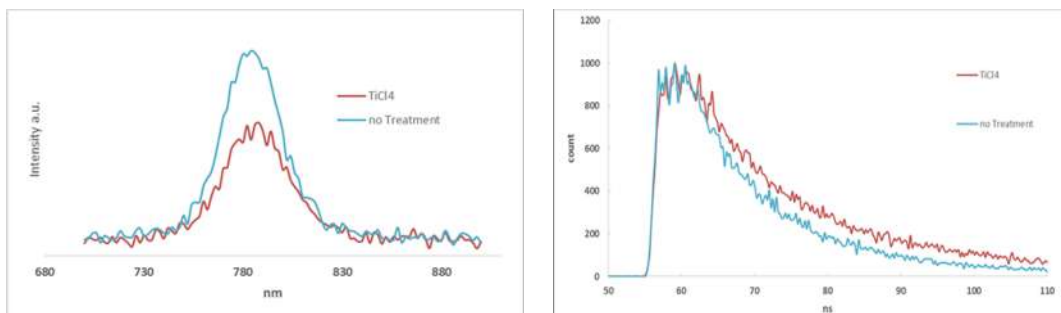

Figure 4.7: Photoluminescence and tr-photoluminescence of treated and untreated solar cell

In order to reduce the time length of the process, it was decide to do the annealing and the calcination phases of the TiO_2 layer using an hot-plate in air (at 500 °C), avoiding the furnace. Thanks to the faster ramp-up and ramp-down of the hot plate temperature, it was possible to save almost 6 hours for each batch of solar cells.

Figure 4.8 shows the result of the solar cells for which the annealing and the calcination of the TiO_2 was done at 500° for 60 min on a hot-plate in air.

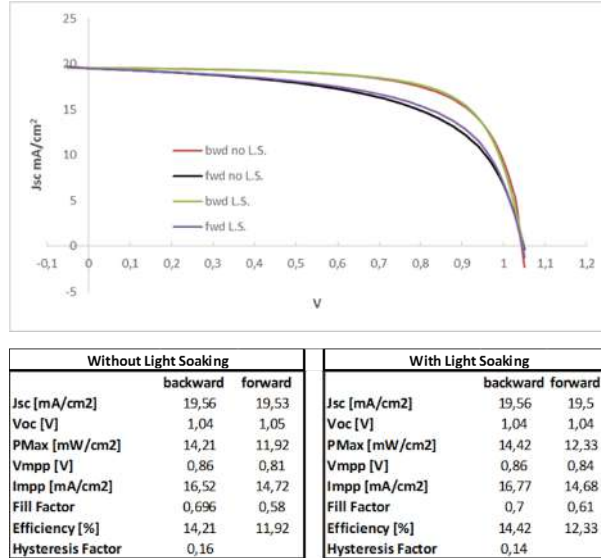| Without Light Soaking			With Light Soaking		
	backward	forward		backward	forward
Jsc [mA/cm2]	19,56	19,53	Jsc [mA/cm2]	19,56	19,5
Voc [V]	1,04	1,05	Voc [V]	1,04	1,04
PMax [mW/cm2]	14,21	11,92	PMax [mW/cm2]	14,42	12,33
Vmpp [V]	0,86	0,81	Vmpp [V]	0,86	0,84
Impp [mA/cm2]	16,52	14,72	Impp [mA/cm2]	16,77	14,68
Fill Factor	0,696	0,58	Fill Factor	0,7	0,61
Efficiency [%]	14,21	11,92	Efficiency [%]	14,42	12,33
Hysteresis Factor	0,16		Hysteresis Factor	0,14	

Figure 4.8: Solar cells fabricated using the hot plate process showed less L.S. effect

An important reduction of the hysteresis was observed. The V_{oc} enhanced compared with previous samples. Measuring the solar cells under continuous illumination, it was noted that they are not influenced by the light soaking effect. At the time this experiment was done, some assumptions were made concerning the difference in performances between the "hot-plate process" and the "furnace process".

Firstly, light can influence the TiO_2 crystals growth: Nakajima et al. [46] reported how crystals nucleation of oxide films is affected by photochemical reactions due to different light source (pulsed, continuous, and so on) and temperature conditions. In our study, the TiO_2 films remain in the dark being inside the furnace, while using the hot-plate they were exposed to ambient light.

Secondly, oxygen pressure condition can affect the concentration of oxygen vacancies of the compact layer (TiO_{2-x}). Gobaut et al. [47] reported that vacancies in the compact layer act like donors in n-type semiconductors, influence the band gap value. Considering our case, inside the closed ambient of the furnace it is supposed to be less oxygen, with consequently more vacancies in the ETL. On the contrary, when annealing and calcination are done in air, the TiO_2 layer should have less oxygen vacancies.

Last hypothesis concerns the effect of the temperature ramp-up and ramp-down have on the grains growth of the TiO_2. Indeed, while the hot-plate requires 8 min to reach 500 °C

and 20 min for cooling down until 50 °C, the furnace requires 30 min for reaching 500 °C and more than 3 hours for cooling down at 50 °C.

In order to investigate about these hypothesis, further studies were proposed. A furnace with controlled atmosphere and a complete characterization using transmission electron microscopy (TEM), and ultraviolet and X-Ray Photoelectron Spectroscopy (UPS and XPS) should provide more and accurate information about the film growth, crystal structure, and surface quality.

Since good results and reproducibility was achieved, the solar cells fabricated using the $TiCl_4$ treatment (hot plate annealing) will be considered from now as baseline for all the other tests performed.

4.3 Mg-doped TiO_2 compact layer

Among the ways for improving the performance of perovskite solar cells, doping of TiO_2 results is very promising. It can easily enhance the electron transfer properties of material [48]. Previous studies, especially concerning Dye Sensitive Solar Cells [49], showed that Mg can improve the photoactivities of TiO_2 anatase. Iwamoto et al. [50] reported that Mg can shift upward the conduction band of TiO_2 leading better matching of the conduction band between TiO_2 and $MAPbI_3$ increasing the V_{oc}. Furthermore, it was also demonstrated that Mg doping could suppress trap states in anatase TiO_2 [51].

For this work, $Mg(NO_3)_2 6H_2O$ (Wako Pure Chemical Industries, Ltd.) was dispersed by ultrasonification in a solution of TiAcAc and Ethanol (1:10 vol. ratio) at five different concentration: 10 mM, 5 mM, 1 mM, $5x10^{-1}$ mM, $1x10^{-1}$ mM.

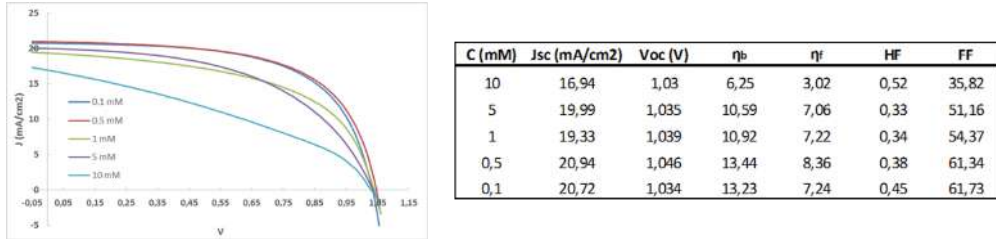| C (mM)	Jsc (mA/cm2)	Voc (V)	η_b	η_f	HF	FF
10	16,94	1,03	6,25	3,02	0,52	35,82
5	19,99	1,035	10,59	7,06	0,33	51,16
1	19,33	1,039	10,92	7,22	0,34	54,37
0,5	20,94	1,046	13,44	8,36	0,38	61,34
0,1	20,72	1,034	13,23	7,24	0,45	61,73

Figure 4.9: J-V curves at different Mg-doping concentration

Figure 4.9 shows comparative J-V backward curves for different concentration of Mg. We expected Mg-doped TiO_2 exhibited a much longer electron life time and a smaller contact resistance, indicating a reduced recombination of electrons and holes which makes an improvement of both the V_{oc} and the J_{sc} [52]. With 0.5 mM of Mg, the V_{oc} increased to 1.046 V, J_{sc} increased to 20.94 mA/cm^2, with a Fill Factor of 61.34%. As HF indicates, hysteresis behavior does not seem to be affected as much as expected, even if a slight reduction was observed with decreasing the Mg concentration.

All the parameters decrease when the concentration of Mg is increased. With a concentration of 10 mM the Voc measured was 1.03 V and the solar cell was exhibiting poor performances and the highest hysteresis. From the J-V curves is clearly visible that series

resistances are reducing the FF.

Figure 4.10 compares SEM of Mg-doped and $TiCl_4$ samples. Morphology of the two samples did not show any notable differences. The we analyze the doped sample and the baseline one using the Grazing Incidente XRD for FTO/TiO_2 structures and $\theta/2\theta$ for PSCs. The comparable FWHM pointed out that crystallinity of ETL is not affecting the results. The XRD diffractograms of the solar cells were approximately equivalent. This means that neither the perovskite crystallinity structure was influencing the performance of the devices.
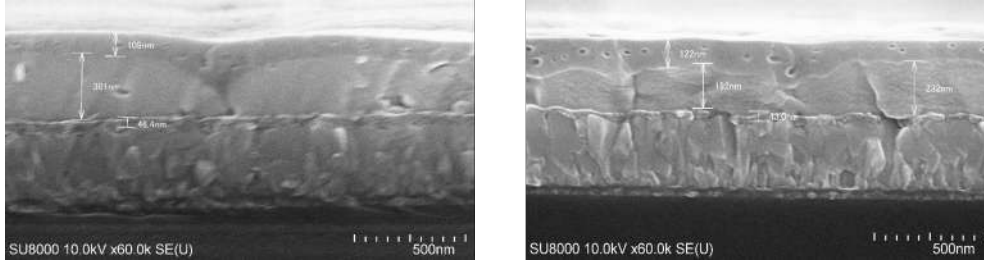

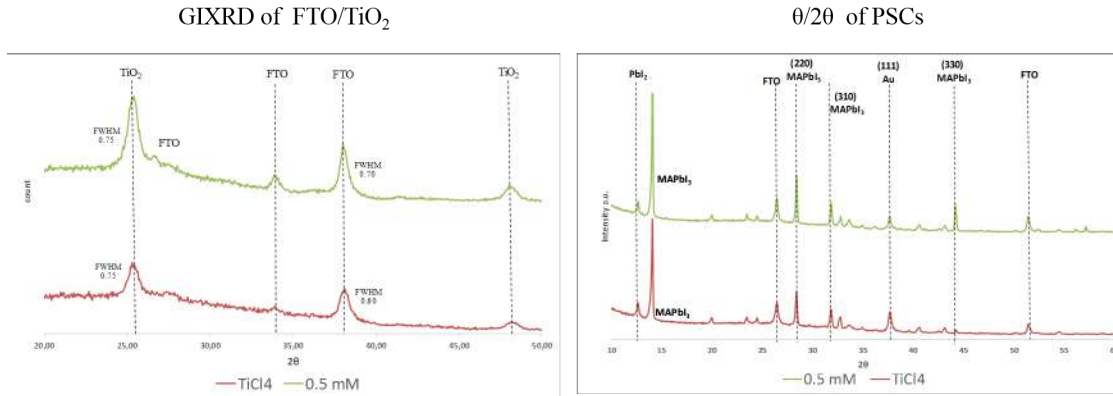Figure 4.10: SEM of Mg-doped solar cell (on the left) and $TiCl_4$ treated solar cell (on the right)

Figure 4.11: GIXRD and $\theta/2\theta$ XRD for FTO/TiO_2 structures and for complete solar cell comparing Mg doping and $TiCl_4$ treatment

To further investigate about these results, we decide to measure the photoluminescence and absorption spectra of different TiO_2 coated on bare glass substrate.

In figure 4.12b the photoluminescence spectra of five different samples are compared. The PL characterization tool could measure a wavelength of 3.2 eV as maximum.

The main issue we faced with these measurements, was the emitting spectra of the bare glass substrate around 2.1 eV. The laser used for the PL, had a slightly higher energy compared to the band gap of TiO_2. Thus, was not possible to distinguish between the
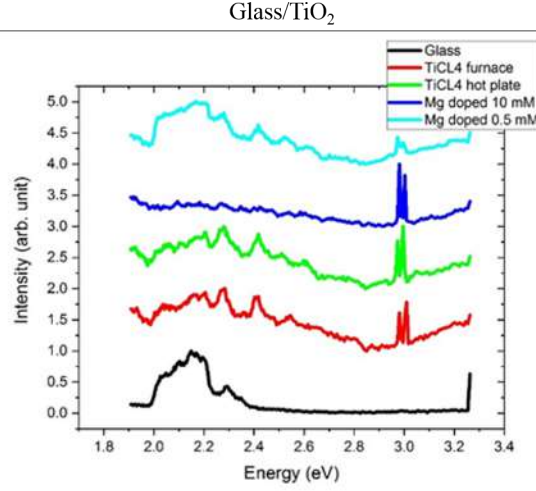
35

Figure 4.12: Photoluminescence spectra comparing TiCl$_4$ treatment and Mg-doping

laser signal and the TiO$_2$ band to band signal. The PL band from 2.4 to 3.1 eV can be divided in two parts. The first one from 2.8 to 3.1 eV where high intensity peaks appear. Some authors attributed these band emissions to surface states and defects [53]. The second region is from 2.4 to 2.8 eV and the peaks are related with bulk impurities. These bulk impurities, mainly in the form of oxygen defects, always act as the centers of non-radiative recombination [53]. Figure 4.13 shows the absorption spectra of the different Mg doping concentration and TiCl$_4$ samples coated on bare glass. 10 and 1 mM show stronger absorption below their band gap (at higher wavelengths). This is related to poin defects within the TiO$_2$ that act as non radiative recombination. TEM could help for understanding the internal microstructure of ETL studied.

As preliminary study, the band gap of the different compact layer was evaluated using the absorption spectra and the formula

$$E(eV) = \frac{hC}{\lambda_{co}}$$

where h is the Planck's constant and C the light speed. The value of λ_{co} is the *wavelength cut-off*, a wavelength above which the absorbance is not due to band to band absorption [54]. This value was obtained fitting the data of the absorption coefficient at high energy with a linear curve. The intersection between this curve and the x-axis is the λ_{co} (fig 4.14). As expected, the band gap of TiO$_2$ is enlarged as consequence of the Mg-doping treatment.
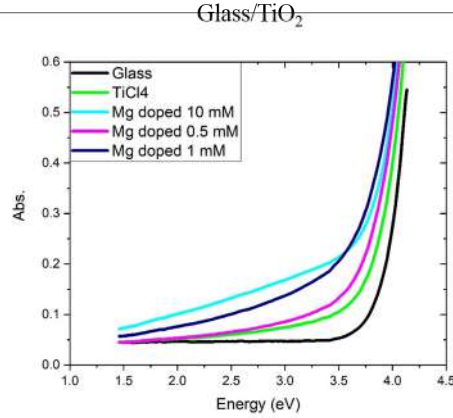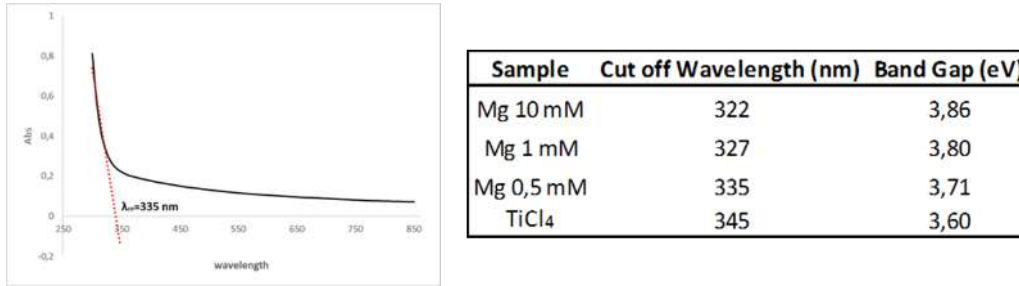
Figure 4.13: Absorption spectra for different Mg-doping concentration

Sample	Cut off Wavelength (nm)	Band Gap (eV)
Mg 10 mM	322	3,86
Mg 1 mM	327	3,80
Mg 0,5 mM	335	3,71
TiCl4	345	3,60

Figure 4.14: The cut off wavelentgh and the band gap of TiO_2

4.4 Al_2O_3 surface passivation

One of the most used techniques to suppress the interfacial recombination of TiO_2 layers is the surface passivation by metal oxides [55].

Among several oxides such as ZnO, ZrO_2, MgO, Nb_2O_5, typically studied and used for DSCs, Al_2O_3 is one of the most commonly used surface passivation materials on TiO_2 in PCSs. Due to its insulator nature (band gap around 8.8 eV [55]), it can work efficiently only when the metal oxide layer used is extremely thin to allow carriers to tunnel throw it. As explained in the previous chapter, the atomic layer deposition method is the suitable because of its property to deposit conformal, pinhole-free coatings with precise thickness control to the atomic scale.

Even if the ALD functioning is based on sequential self-limiting surface reactions, it might happen that residual impurities affect the film deposited during the final application. The origin of this problem is the incomplete removal of precursor ligands. Some authors found that hydrogen coming from the precursors (TMA and H_2O in this study) is one of the main contaminants during the films deposition by ALD [56]. To solve this, a reduction of

hydrogen-contamination concentration seems to be relevant in preparation of high-quality films [56].

In the present study, we studied 3 different thickness of Al_2O_3, depending on the number of the ALD cycles. Ten cycles corresponds to $\approx$1 nm. The samples were exposed to two different exposure time (defined as high and low exposure) of the oxidant precursor. The main differences between high and low exposure mode are the amount of precursors interaction with the substrate (controlled by the Mass Flow Control MFC) and the delay time between the two precursors.
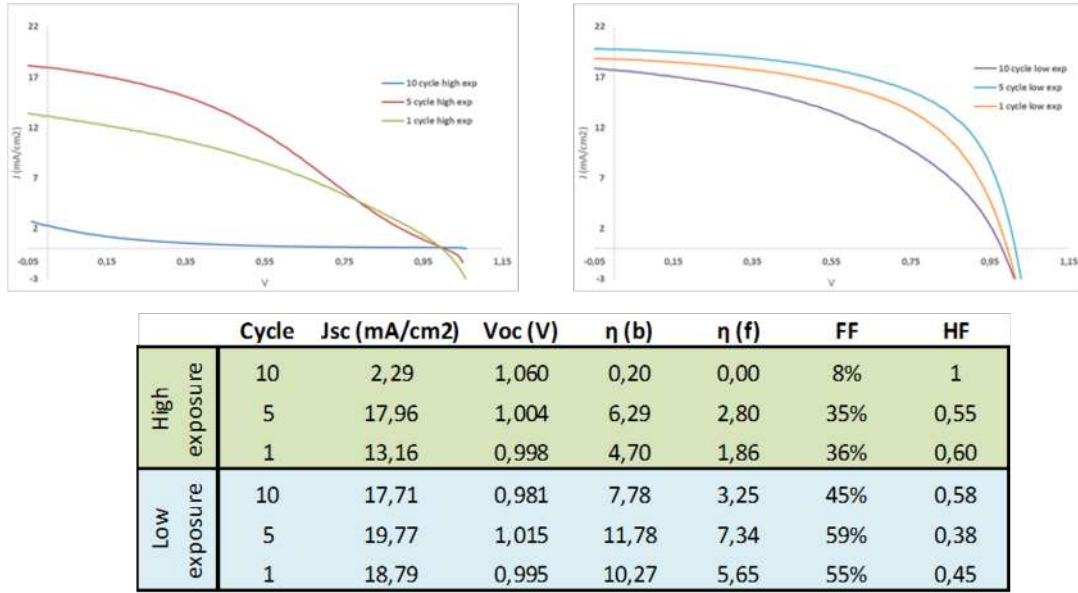

	Cycle	Jsc (mA/cm2)	Voc (V)	η (b)	η (f)	FF	HF
High exposure	10	2,29	1,060	0,20	0,00	8%	1
	5	17,96	1,004	6,29	2,80	35%	0,55
	1	13,16	0,998	4,70	1,86	36%	0,60
Low exposure	10	17,71	0,981	7,78	3,25	45%	0,58
	5	19,77	1,015	11,78	7,34	59%	0,38
	1	18,79	0,995	10,27	5,65	55%	0,45

Figure 4.15: J-V curves of PSCs treated with Al_2O_3 surface passivation (high and low exposure method)

Initially only the high exposure mode was tested. As shown in figure 4.15, increasing the number of ALD cycles (around 1 nm), a dense Al_2O_3 layer is deposited. It was unsuitable for the solar cell since it completely blocked the charge transfer from the perovskite to TiO_2. The next step was finding the optimal thickness of the Al_2O_3 layer. Thus, 5 and 1 cycle were tested. As the data show, 5 ALD cycles gave the highest performances with J_{sc} 17.96 mA/cm^2 and V_{oc} above 1 V. Fill Factor resulted to be very low compared with the previous experiments, together with a large hysteresis factor. The slope of the curves also suggested very high series resistances and low shunt resistances. As mentioned before, this is probably due to the high concentration of hydrogen that acts as contaminants. Indeed, when it is not completely purged, it prevents the new precursor to fill properly the pinholes (causing low shunt resistances). At the same time, the residual impurities can act as series resistances.

To overcome this problem, the low exposure mode (less amount of precursors) was tested.

The first result was an important improvement compare with the high exposure mode. J_{sc}, backward efficiency, fill factor improved, while the hysteresis factor slightly decreased. The V_{oc} was not affected that much, with values around 1 V. Again, we found out that 5 ALD cycles were the optimum in terms of performances. These studies clearly show that an extremely thin layer is required for the passivation effect, but at the same time a minimum thickness, ≈ 0.5 nm, is required. Figure 4.16 shows the J-V curves for Al_2O_3 treated solar cells and baseline solar cells. These latters still have better performances in terms of efficiency and hysteresis factor. Neither in this case structural characterization made using SEM (fig. 4.17), GIXRD and $\theta/2\theta$ XRD (fig. 4.18) showed no relevant differences in morphology or crystallinity. FWHM and diffractograms were compared.
Figure 4.19 compares the steady-state PL and tr-Pl spectra: $TiCl_4$ PSCs showed a better carrier extraction while the non-radiative recombination is still predominant even after the surface passivation treatment.
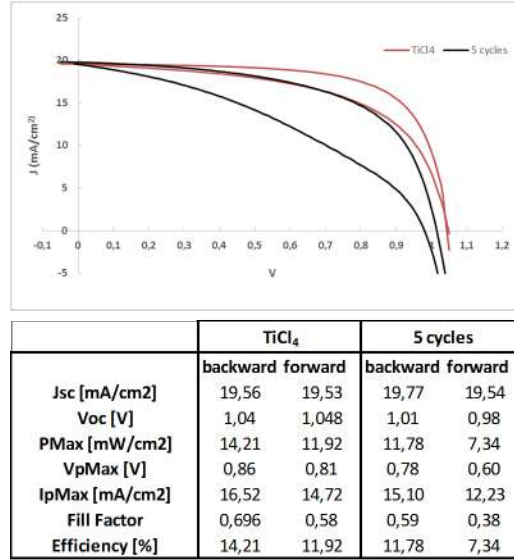

	$TiCl_4$		5 cycles	
	backward	forward	backward	forward
Jsc [mA/cm2]	19,56	19,53	19,77	19,54
Voc [V]	1,04	1,048	1,01	0,98
PMax [mW/cm2]	14,21	11,92	11,78	7,34
VpMax [V]	0,86	0,81	0,78	0,60
IpMax [mA/cm2]	16,52	14,72	15,10	12,23
Fill Factor	0,696	0,58	0,59	0,38
Efficiency [%]	14,21	11,92	11,78	7,34

Figure 4.16: J-V curves of PSCs treated with Al_2O_3 surface passivation and Baseline PSCS
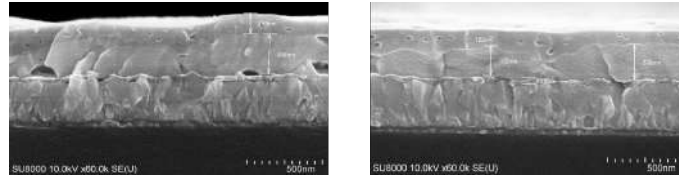

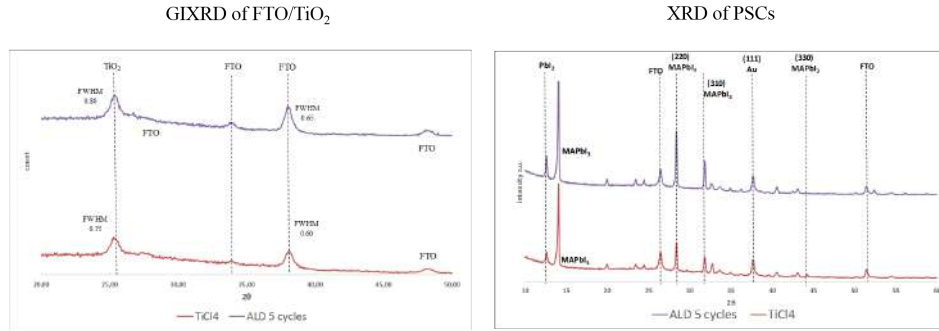Figure 4.17: SEM of Al_2O_3 solar cell (on the left) and $TiCl_4$ baseline solar cell (on the right)

Figure 4.18: GIXRD and $\theta/2\theta$ XRD for FTO/TiO$_2$ structures and for complete solar cell comparing Al$_2$O$_3$ and TiCl$_4$ treatment
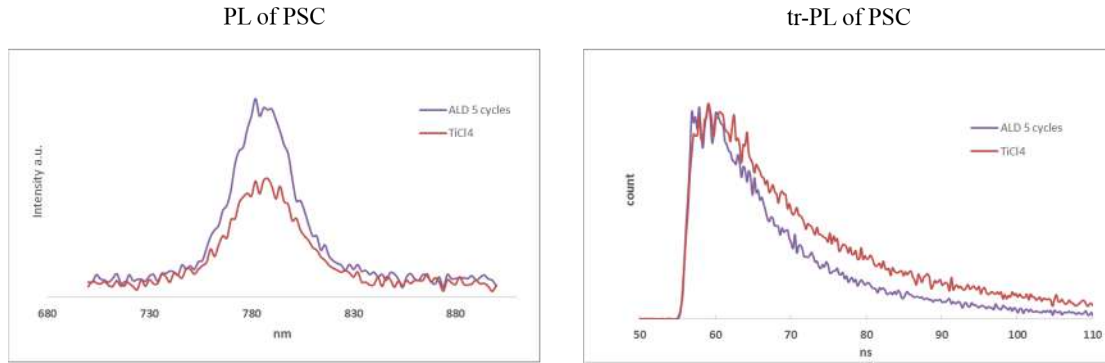

Figure 4.19: Photoluminescence and tr-photoluminescence of treated and untreated solar cells

4.5   Conclusions

In this work, I have been introduced to some processing and characterization techniques used for the development of Perovskite Solar Cells. This technology is a very promising one among the third generation of photovoltaic devices. The main properties and the main technical developments done by several academic groups were presented. I have presented the issues that limit both the efficiency and stability of PSCs (ie thermal, UV-light and atmospheric degradation).

Moreover the hysteretic behavior, mismatch between the forward and backward J-V measurement, seems to be one of the major obstacles for the durability of these devices. Since the hysteresis origin is still not clear and under debate, different probable causes were presented such as ferroelectric property, ion migration, interfacial carrier dynamics and traps state. Following previous studies [27] and recent models [30] we decided to investigate the TiO$_2$ ETL properties and its influence on the PSC efficiency. Two fabrication

processes and different chemical, doping and surface treatments were tested. $TiCl_4$ chemical treatment led to an increase of η_{back} (+52%) and decrease of hysteresis factor (-53%) compared with no-treated solar cells. Light soaking effect was also observed. The results obtained will be the basis for further study on the growth of the TiO_2 layer with controlled atmospheric conditions (oxygen pressure). Doping the ETL with different amount of $Mg(NO_3)_2 6H_2O$ showed an improvement of V_{oc}. Concentration of 0.5 mM and 0.1 mM enhanced the V_{oc} up to 1.046 V and 1.034 V respectively but without decreasing the hysteresis. PL investigation of TiO_2 coated on top of quartz as transparent substrate was proposed in order to avoid signal coming from the glass substrate (which is emitting at the same energy than TiO_2 deep traps). It might allow to have a better understanding of the role the ETL on the PSCs properties . Surface treatment for passivating defects was tested depositing thin Al_2O_3 layer with ALD on top of cp-TiO_2. Using the low exposure mode it was possible to enhance the performance probably due to the reduction of hydrogen concentration as contaminant during the process. The best results were obtained with 5 ALD cycles ($\approx$0.5 nm) using the low exposure mode.

Bibliography

[1]   International Energy Agency. *Snapshot of Global Photovoltaic Markets 2017*. 2017.

[2]   National Renewable Energy Laboratory (NREL). *Best Research-Cell Efficiencies*. 2017. URL: https://www.nrel.gov/pv/assets/images/efficiency-chart.png.

[3]   Gast. P.R. *'Solar radiation', in Campen et al.* 1960, pp. 14–30.

[4]   *Semiconductor Technology from A to Z*. 2017. URL: https://www.halbleiter.org.

[5]   *Photovoltaic Education Network*. 2017. URL: http://www.pveducation.org.

[6]   A. Luque and S. Hegedus. *Handbook of Photovoltaic Science and Engineering, Second Edition*. 2011.

[7]   Dubin S. and Gray J. *IEEE Trans. Electron Devices 41*. 1994, pp. 239–245.

[8]   P. Auger. *Sur les rayons beta secondaires produits dans un gaz par des rayons X*. 1923.

[9]   W. Shockley and W. T. Read. *'Statistics of the Recombinations of Holes and Electrons*. 1952, p. 835.

[10] ElectronicsTutorials. *PN Junction Diode: forward and revers bias*. URL: http://www.electronics-tutorials.ws.

[11] Park N., Grätzel M., and Miyasaka T. *Perovskite Photovoltaics From Fundamentals to Device Architectures*. 2016.

[12] H.J. Snaith. *Perovskites: The Emergence of a New Era for Low-Cost, High-Efficiency Solar Cells*. 2013.

[13] Umari P., Mosconi E., and F. De Angelis. *Relativistic GW calculations on CH3NH3PbI3 and CH3NH3SnI3 perovskites for solar cell applications*. 2014.

[14] Kojima A., Teshima K., and Miyasaka T. Shirai Y. *Organometal halide perovskites as visible-light sensitizers for photovoltaic cells*. 2009.

[15] Lee M. M. et al. *Efficient hybrid solar cells based on meso-superstructured organometal halide perovskites*. 2012.

[16] Moon S-J-Humphry-Baker R. Grätzel M. Burschka J. Pellet N. *Sequential deposition as a route to high-performance perovskite-sensitized solar cells*. 2013.

[17] Matsui T-et al. Saliba M Orlandi S. *A molecularly engineered hole-transporting material for efficient perovskite solar cells*. 2016.

[18] Yang G-et al. Hu H Jiang K. *Terthiophene-Based D–A Polymer with an Asymmetric Arrangement of Alkyl Chains That Enables Efficient Polymer Solar Cells.* 2015.

[19] Blancon J-C et al. Tsai H Nie W. *High-efficiency two-dimensional Ruddlesden–Popper perovskite solar cells.* 2016.

[20] Jiang Y. Soufiani A.M.-Ho-Baillie A. Green M.A. *Optical properties of photovoltaic organic-inorganic lead halide perovskites.* 2015.

[21] De Bastiani M. *The stability of third generation solar cells.* 2016.

[22] M. Darwich-G. E. Eperon H. J. Snaith P. Docampo J. M. Ball. *Efficient organometal trihalide perovskite planar-heterojunction solar cells on flexible polymer substrates.* 2013.

[23] A. F. Carley E. Carter and D. M. Murphy. *Evidence for O2- Radical Stabilization at Surface Oxygen Vacancies on Polycrystalline TiO2.* 2013.

[24] T. Miyasaka A. K. Jena. *Hysteresis Characteristics and Device Stability.* 2016.

[25] Jang I.-H. Ahn-N. Choi M. Guerrero A. Bisquert J. Park N.-G Kim H.-S. *Control of I-V Hysteresis in CH3NH3PbI3 Perovskite Solar Cell.* 2015.

[26] Malliakas C.D. Kanatzidis-M.G. Stoumpos C.C. *Semiconducting tin and lead iodide perovskites with organic cations: phase transitions, high mobilities, and near-infrared photoluminescent properties.* 2013.

[27] Abate A. Eperon-G.E. Leijtens-T. Stranks S.D. Wang J.T.-W. Zhang W. Snaith H.J. *Anomalous hysteresis in perovskite solar cells.* 2014.

[28] Ma F. deQuilettes-D.W. Vorpahl-S.M. Glaz M.S. Colbert A.E.-Ziffer M. E. Ginger-D.S Nagaoka H. *Zr incorporation into TiO2 electrodes reduces hysteresis and improves performance in hybrid perovskite solar cells while increasing carrier lifetimes.* 2015.

[29] A.K. Jena et al. *The interface between FTO and the TiO2 compact layer can be one of the origins to hysteresis in planar heterojunction perovskite solar cells.* 2015.

[30] Samy Almosn et al. *Tunneling-Assisted Trapping as one of the Possible Mechanisms for the Origin of Hysteresis in Perovskite Solar Cells.* 2017.

[31] K. Emery, D. Myers, and S. Rummel. *Solar simulation - problems and solutions.* 1988.

[32] Debbie J. Stokes. *Principles and Practice of Variable Pressure Environmental Scanning Electron Microscopy (VP-ESEM).* 2008.

[33] Purdue University. *Scanning Electron Microscope - Radiological and Environmental Management.* 2008. URL: https://www.purdue.edu/ehps/rem/rs/sem.htm.

[34] Andre Guinie. *X-ray Crystallographic Technology.* 1952, p. 271.

[35] Georgia State University. *Hyperphysics.* 2016. URL: http://hyperphysics.phy-astr.gsu.edu/hbase/hph.html.

[36] Claus F. Klingshirn. *Semiconductor Optics.* 2012.

[37] Douglas A. Skoog, F. James Holler, and Stanley R. Crouch. *Principles of Instrumental Analysis (6th ed.)* 2007.

[38] Johnson Richard W., Hultqvist Adam, and F. Bent Stacey. *A brief review of atomic layer deposition: from fundamentals to applications.* 2014.

[39] Hans-Jurgen Butt; Karlheinz Graf; Michael Kappl. *Physics and Chemistry of Interfaces (Third, Revised ed.)* 2013.

[40] S.i Arman and N. M.i Hoda. *Influence of TiCl4 Treatment on Structure and Performance of Dye-Sensitized Solar Cells.* 2013.

[41] Cojocaru L. et al. *Surface Treatment of the Compact TiO2 Layer for Efficient Planar Heterojunction Perovskite Solar Cells.* 2015.

[42] Conings B. et al. *An easy-to-fabricate low-temperature TiO2 electron collection layer for high efficiency planar heterojunction perovskite solar cells.* 2014.

[43] S. D. et al. Stranks. *Recombination kinetics in organic–inorganic perovskites: excitons, free charge, and subgap states.* 2014.

[44] Heo J. H. et al. *Hysteresis-less mesoscopic CH3NH3PbI3 perovskite hybrid solar cells by introduction of Li-treated TiO 2 electrode.* 2015.

[45] Shao S. et al. *Elimination of the light soaking effect and performance enhancement in perovskite solar cells using a fullerene derivative.* 2016.

[46] Nakajima Tomohiko, Shinodaa Kentaro, and Tetsuo Tsuchiyaa. *UV-assisted nucleation and growth of oxide films from chemical solutions.* 2014.

[47] Gobaut B., Sambri P. Orgiani A., and Panaccione G. *Role of Oxygen Deposition Pressure in the Formation of Ti Defect States in TiO2 Anatase Thin Films.* 2017.

[48] Imahori Hiroshi, Ngamsinlapasathian Supachai, and Yoshikawa Susumu. *Comparison of Electrode Structures and Photovoltaic Properties of Porphyrin-Sensitized Solar Cells with TiO2 and Nb, Ge, Zr-Added TiO2 Composite Electrodes.* 2006.

[49] Van Nam Tran, N. T. Trang, and Cong B. T. *Mg-doped TiO2 for Dye-Sensitive solar cell: an electronic structure study.* 2012.

[50] Iwamoto S. et al. *Fabrication of dye-sensitized solar cells with an open-circuit photovoltage of 1 V.* 2008.

[51] Gaoa Linjie et al. *Passivation of defect states in anatase TiO2hollow spheres with Mgdoping: Realizing efficient photocatalytic overall water splitting.* 2017.

[52] Wang J. et al. *Performance enhancement of perovskite solar cells with Mg-doped TiO2 compact film as the hole-blocking layer.* 2015.

[53] Liu Baoshun and Xiujian Zhao Liping Wen and. *The photoluminescence spectroscopic study of anatase TiO2 prepared by magnetron sputtering.* 2006.

[54] Dharma Jayant and Pisal Aniruddha. *Simple Method of Measuring the Band Gap Energy Value of TiO2 in the Powder Form using a UV/Vis/NIR Spectrometer.* 2009.

[55]   Lee Yong Hui et al. *Enhanced Charge Collection with Passivation Layers in Per-ovskite Solar Cells.* 2016.

[56]   Kozen A.C., Schroeder M.A., and Rubloff G.W. *Examining the role of hydrogen in the electrical performance of in situ fabricated metal–insulator– metal trilayers using an atomic layer deposited Al2O3 dielectric.* 2013.

[57]   Mancini Matteo and Ferranti Ludovico. *Passivation of defects for high efficiency planar perovskite solar cells.* 2017, p. 107.